nature cell biology

# Apical–basal polarity inhibits epithelial–mesenchymal transition and tumour metastasis by PAR-complex-mediated SNAI1 degradation

Hae-Yun Jung[1], Laurent Fattet [ID][1], Jeff H. Tsai[1], Taketoshi Kajimoto[1], Qiang Chang[2], Alexandra C. Newton[1] and Jing Yang [ID][1,3]*

Loss of apical–basal polarity and activation of epithelial–mesenchymal transition (EMT) both contribute to carcinoma progression and metastasis. Here, we report that apical–basal polarity inhibits EMT to suppress metastatic dissemination. Using mouse and human epithelial three-dimensional organoid cultures, we show that the PAR–atypical protein kinase C (aPKC) polarity complex inhibits EMT and invasion by promoting degradation of the SNAIL family protein SNAI1. Under intact apical–basal polarity, aPKC kinases phosphorylate S249 of SNAI1, which leads to protein degradation. Loss of apical–basal polarity prevents aPKC-mediated SNAI1 phosphorylation and stabilizes the SNAI1 protein to promote EMT and invasion. In human breast tumour xenografts, inhibition of the PAR-complex-mediated SNAI1 degradation mechanism promotes tumour invasion and metastasis. Analyses of human breast tissue samples reveal negative correlations between PAR3 and SNAI1 protein levels. Our results demonstrate that apical–basal polarity functions as a critical checkpoint of EMT to precisely control epithelial–mesenchymal plasticity during tumour metastasis.

The majority of human carcinomas show a loss of epithelial apical–basal polarity during the progression from benign to invasive carcinoma. Apical–basal polarity is often regarded as a gatekeeper against tumour development and metastasis[1,2]. Apical–basal polarity is regulated by three major polarity complexes: the PAR, Crumbs and Scribble complexes[3–5]. The core PAR complex consists of PAR3, PAR6 and atypical PKCs (aPKCs) and is essential in defining the apical domain of an epithelial cell[6–8]. Binding between PAR6 and aPKCs, PKCζ or PKCι promotes aPKCs to adopt an active and signalling-competent conformation to phosphorylate their substrates[9]. The loss of PAR3 results in dissociation of the PAR complex and a loss of epithelial polarity[10–12]. PAR3 expression is frequently downregulated in the primary tumour of various carcinoma types[1,2,13].

Epithelial–mesenchymal transition (EMT) provides stationary carcinoma cells the ability to invade and disseminate during metastasis[14–16]. During EMT, epithelial cells first lose apical–basal polarity before weakening cell–cell junctions and rearranging the cytoskeleton to acquire invasive capacities. This complex cellular program is orchestrated by the coordinated activation of transcription factors, including the SNAIL, TWIST and ZEB families[17–20]. SNAI1 is a key factor in suppressing E-cadherin expression and promoting loss of epithelial characteristics, including epithelial polarity and junctions[21–23].

Recent studies show that carcinoma cells undergo EMT to disseminate, whereas turning off EMT is needed for metastatic outgrowth[24–26]. Although microenvironmental cues, including inflammation, hypoxia and matrix stiffness, are implicated in the regulation of epithelial–mesenchymal plasticity[27,28], very little is known about whether any intrinsic cellular machineries, such as apical–basal polarity and cell–cell junctions, could directly impinge

on EMT transcription factors to control EMT progression. Here, we employ three-dimensional (3D) epithelial organoid cultures that retain the integrity of apical–basal polarity in epithelial tissues to explore the molecular links between epithelial cell polarity and EMT transcription factors and to define the impact of this feedback mechanism linking the PAR polarity complex and the SNAI1 transcription factor in tumour invasion and metastasis.

## Results

**SNAI1 protein is destabilized and fails to induce EMT in 3D primary mouse MEOs.** To determine the impact of apical–basal polarity on EMT progression, we employed a 3D organoid culture in which freshly isolated primary mouse mammary epithelial organoids (MEOs) form a bilayer ductal structure composed of the luminal and basal cell layers with a centrally localized hollow lumen, membranous E-cadherin and cortical F-actin at the apical side[29] (Fig. 1a). We isolated primary MEOs from the tetracycline-inducible *SNAI1* (TetON-Snai1) mice we generated. In two-dimensional (2D) cultures, TetON-Snai1 mammary epithelial cells (MECs) formed a monolayer with intact E-cadherin-mediated adherens junctions. Following the induction of SNAI1, these cells switched to a spindle-like cell shape and displayed many EMT features, including reduced E-cadherin-mediated adherens junctions and increased fibronectin expression, within four days (Fig. 1b). In 3D cultures, MEOs formed a hollow lumen and complete apical–basal polarity (Fig. 1b). Surprisingly, these MEOs retained their acinar structure with intact adherens junctions following SNAI1 induction (Fig. 1b). Consistent with these phenotypes, SNAI1 induction resulted in E-cadherin messenger RNA suppression and vimentin mRNA expression in 2D, but not 3D, cultures (Supplementary Fig. 1a). As a positive control, we also isolated primary MEOs from the
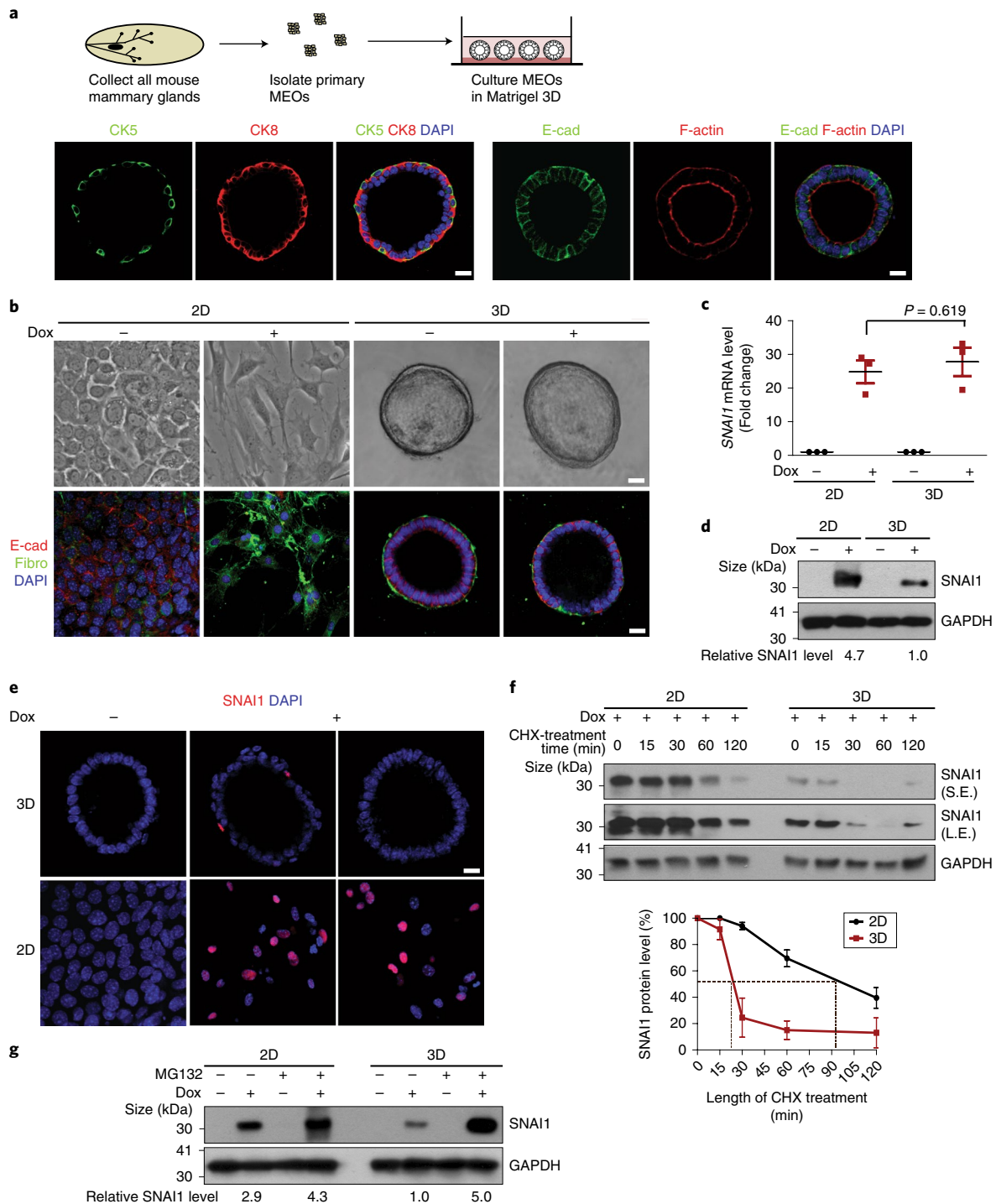
**Fig. 1 | SNAI1 protein is unstable and fails to induce EMT in MEOs with intact apical–basal polarity. a**, Experimental scheme for isolating and culturing primary mouse MEOs (top). Immunofluorescence images for cytokeratin 8 (CK8), cytokeratin 5 (CK5), E-cadherin (E-cad) and F-actin in MEOs after four days of culture (bottom). **b**, Bright-field (top) and immunofluorescence (bottom) images for E-cadherin and fibronectin (Fibro) in TetON-Snai1 3D MEO and 2D MEC cultures before and after doxycycline (Dox) treatment for four days. **c**, Quantitative PCR (qPCR) analysis of relative *SNAI1* mRNA levels normalized to *GAPDH* in TetON-Snai1 MECs and MEOs before and after doxycycline induction. $n = 3$ independent experiments; unpaired two-tailed Student's $t$-test with Welch's correction. **d**, Immunoblots for SNAI1 and GAPDH in the lysates from TetON-Snai1 MECs and MEOs before and after four days of doxycycline treatment. The values indicate the signal intensities of SNAI1 relative to GAPDH. **e**, Immunofluorescence images for SNAI1 in TetON-Snai1 MEOs and MECs before and after four days of doxycycline induction. **f**, TetON-Snai1 MECs and MEOs were treated with doxycycline for four days, followed by 10 μM cycloheximide (CHX) for the indicated time periods and analysed for SNAI1 and GAPDH by immunoblotting (top). The graph represents the SNAI1 levels relative to GAPDH (bottom). Dashed lines represent Snai1 protein half-life (50% of the maximum Snai1 protein level). S.E., short exposure; L.E., long exposure. $n = 3$ independent experiments. **g**, TetON-Snai1 MECs and MEOs were treated with doxycycline for four days, followed by 10 μM MG132 for 4 h and analysed for SNAI1 and GAPDH by immunoblotting. The values indicate the signal intensity of SNAI1 relative to GAPDH. All of the immunofluorescence and western blot images shown represent one of three independent experiments. Scale bars, 25 μm. Error bars represent the s.d. The source data for the graphs can be found in Supplementary Table 3 and unprocessed blots in Supplementary Fig. 7.

TetON-Twist1 mice we previously generated[25]. Induction of TWIST1 in 3D MEOs and 2D MECs isolated from these TetON-Twist1 mice both resulted in EMT and single cell invasion (Supplementary Fig. 1b–d), which is consistent with published data[30]. Together, these data show that in contrast to TWIST1, SNAI1 induction fails to promote EMT specifically in 3D polarized organoids.

We then examined the *SNAI1* mRNA and protein levels in 2D and 3D cultures. Doxycycline treatment induced *SNAI1* mRNA to similar levels in 2D and 3D cultures (Fig. 1c). However, a significantly lower level of SNAI1 protein was detected in MEOs compared with MECs (Fig. 1d). Consistent with this, SNAI1 protein was detectable in only very few epithelial cells in MEOs, whereas the majority of MECs expressed SNAI1 protein after doxycycline treatment (Fig. 1e). In contrast, TWIST1 protein and mRNA could be easily detected in TetON-Twist1 MEOs as well as in TetON-Twist1 MECs (Supplementary Fig. 1e,f). These results show that despite potent induction of *SNAI1* mRNA, SNAI1 protein levels failed to increase in 3D polarized MEOs.

We examined SnaiNAI1 protein degradation rates in 2D versus 3D cultures in the presence of cycloheximide. Interestingly, SNAI1 protein was remarkably unstable in MEOs with a half-life of around 20 min compared with >100 min in MECs (Fig. 1f). Treatment with the proteasome inhibitor MG132 increased the SNAI1 protein level in MEOs to a level similar to MECs (Fig. 1g). Together, these results show that SNAI1 protein stability is significantly reduced in 3D polarized MEOs, which might be responsible for the failure of SNAI1 to promote EMT.

**Loss of apical–basal polarity increases SNAI1 stability in MEOs.** One major difference between 3D MEOs and 2D MECs is the apical–basal polarity. We therefore reasoned that polarity might directly regulate SNAI1 protein stability. Primary MEOs took three days to establish a hollow lumen and apical–basal polarity, as indicated by the presence of cortical F-actin and the PAR complex components PAR3 and PKCζ at the apical surface. In contrast, after one day of culture, the majority of MEOs were not polarized with filled lumen (Fig. 2a and Supplementary Fig. 2a). Induction of SNAI1 in these pre-polarized MEOs resulted in a significantly higher percentage of organoids undergoing EMT (Fig. 2b), as indicated by reduced E-cadherin-mediated adherens junctions, loss of laminin V-positive basement membrane and increased fibronectin expression compared with induction of SNAI1 in polarized MEOs (Fig. 2c). Furthermore, SNAI1 protein levels increased in pre-polarized MEOs compared with polarized MEOs after doxycycline treatment (Fig. 2c–e), supporting a role for apical–basal polarity in regulating SNAI1 protein levels.

We also used a selective myosin light-chain kinase inhibitor (ML7) to disrupt apical–basal polarity in fully polarized MEOs, as previously reported[31,32]. Notably, ML7 treatment disrupted apical–basal polarity, greatly increased the percentage of SNAI1-positive cells in individual MEOs (Fig. 2f,g) and increased the total SNAI1 protein level (Fig. 2h). Together, our results strongly indicate that apical–basal polarity negatively regulates SNAI1 protein stability.

**aPKC-mediated SNAI1 phosphorylation promotes SNAI1 protein degradation.** Previous studies reported that SNAI1 stability is regulated by the phosphorylation of SNAI1 protein by GSK3β[33,34]. Treatment with a selective GSK3 inhibitor CHIR-99021 increased SNAI1 protein levels in 2D MECs and in 3D MEOs; however, the fold increases in the SNAI1 protein levels were similar in 2D MECs and 3D MEOs, and the SNAI1 protein level remained significantly lower in 3D MEOs compared with that in 2D MECs following GSK3β inhibition (Supplementary Fig. 3a). Together, these data suggest that GSK3β is not responsible for apical–basal polarity-induced SNAI1 degradation.

To uncover the unknown mechanisms regulating SNAI1 protein stability, we used protein modification prediction software packages to identify potential conserved phosphorylation sites on SNAI1. These analyses identified S249 as a candidate aPKC phosphorylation site (Supplementary Fig. 3b,c). Sequence alignment showed that the potential aPKC phosphorylation motif RMSLL is highly conserved from humans to *Drosophila* (Fig. 3a). Atypical PKCs serve as core components of the PAR polarity complex that is essential for apical–basal polarity[35]. We therefore generated phospho-deficient S249A and phospho-mimetic S249E SNAI1 mutants to determine whether phosphorylation of S249 affects SNAI1 protein stability. Indeed, the steady-state levels of the S249E SNAI1 mutant protein were significantly lower than those of the wild-type (WT) or S249A mutant SNAI1 (Fig. 3b); in contrast, their mRNA levels were similar in 2D cultures of MCF10A cells without apical–basal polarity (Fig. 3c). The S249E SNAI1 protein consistently displayed a shorter half-life compared with WT or S249A SNAI1 proteins (Fig. 3d). MG132 stabilized the S249E SNAI1 protein without affecting its mRNA level (Fig. 3e,f). Furthermore, compared with WT SNAI1 and S249A mutant protein, the S249E mutant protein was highly ubiquitinated in the absence or presence of MG132 (Fig. 3g), further supporting the notion that phosphorylation of SNAI1 at S249 promotes SNAI1 ubiquitination and proteasome-mediated protein degradation.

To directly test whether aPKCs could phosphorylate S249 on SNAI1, we performed an in vitro kinase assay, using a phopho-S249-specific SNAI1 antibody that we generated, and found that purified PKCζ could phosphorylate purified SNAI1 WT protein at S249. Importantly, S249 phosphorylation was inhibited in the presence of the aPKC-specific inhibitor PZ09 (ref. [36]; Fig. 3h). We next co-expressed SNAI1 and PKCζ with β-TrCP, the E3 ligase that is predicted to bind to the S249 region. Ubiquitination of SNAI1 was detected in cells co-expressing PKCζ and β-TrCP and was reversed by treatment with PZ09 (Fig. 3i). Furthermore, we tested the SNAI1-6AS mutant in which all GSK3β-phosphorylation sites are abolished[34] and found that this mutant is as responsive to aPKC-mediated SNAI1 degradation as the WT SNAI1 protein (Supplementary Fig. 3d). These results show that phosphorylation of SNAI1 at S249 by aPKCs reduces SNAI1 protein stability, which is independent of GSK3-mediated SNAI1 phosphorylation.

We next expressed Tet-inducible SNAI1 WT and S249 mutants in polarized MEOs by lentiviral infection. Using a lentiviral construct carrying green fluorescent protein (GFP), we determined that our primary organoid infection reached about 35% of cells in individual organoids (Supplementary Fig. 2b). Similar to what we observed in TetON-Snai1 MEOs, the majority of organoids overexpressing WT SNAI1 and the S249E mutant failed to undergo EMT and invasion following doxycycline induction; in contrast, the S249A mutant was able to induce EMT and invasion in more than 65% of polarized organoids (Fig. 4a,b). The S249A mutant, but not WT and S249E SNAI1, consistently showed higher protein expression in MEOs without affecting *SNAI1* mRNA levels (Fig. 4c,d). Together, these data suggest that apical–basal polarity regulates S249 phosphorylation to impact SNAI1 protein degradation and EMT.

**The PAR3–aPKC complex is required for apical–basal polarity-induced SNAI1 protein degradation.** To determine whether aPKC kinase activity is required for SNAI1 protein degradation in polarized MEOs, we treated TetON-Snai1 MEOs with PZ09, which inhibits both PKCζ and PKCι. In MEOs with intact apical–basal polarity, PKCζ and PAR3 could be detected at the apical region, as marked by strong cortical F-actin signals (Fig. 4e). Importantly, induction of SNAI1 in the presence of PZ09 effectively promoted EMT in more than 80% of the MEOs, compared with activation of EMT in less than 15% MEOs in the control group (Fig. 4e,f). Furthermore, PZ09 treatment drastically increased SNAI1 protein
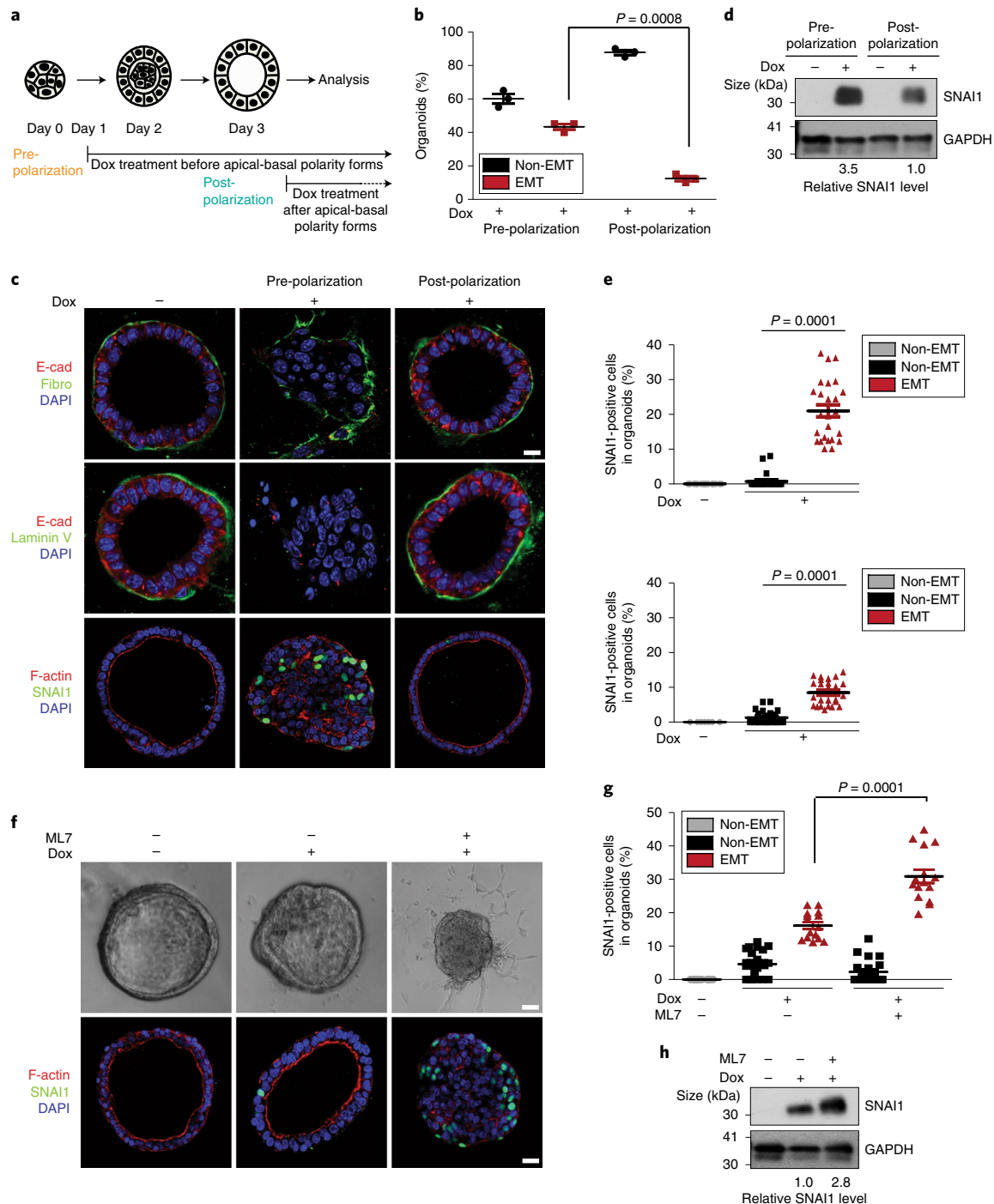
**Fig. 2 | Disruption of apical–basal polarity increases SNAI1 protein stability in MEOs. a**, Experimental scheme for the induction of SNAI1 in organoids before and after polarization. **b**, Quantification of the percentage of MEOs undergoing EMT under pre- and post-polarization conditions. Unpaired two-tailed Student's *t*-test with Welch's correction; *n* = 3 independent experiments with 50 organoids per condition in each experiment. **c**, Immunofluorescence images for E-cadherin, fibronectin, laminin V, SNAI1 and F-actin in TetON-Snai1 MEOs pre- and post-polarization, as indicated. **d**, Immunoblot for SNAI1 and GAPDH from TetON-Snai1 MEOs under pre-and post-polarization conditions, as indicated. The values indicate the SNAI1 signal intensities relative to GAPDH. **e**, Percentage of SNAI1-positive cells in TetON-Snai1 MEOs under pre-polarization (top; *n* = 20 and 25 cells for the Dox− and Dox+ groups, respectively) and post-polarization (bottom; *n* = 20 cells for the Dox− and Dox+ EMT groups, *n* = 25 cells for the Dox+ non-EMT group) conditions as indicated. Data represent one of three independent experiments. Unpaired Student's two-tailed *t*-tests with Welch's correction. **f**, Bright-field (top) and immunofluorescence (bottom) images for SNAI1 and F-actin of TetON-Snai1 MEOs treated with doxycycline and 10 μM ML7 for four days. **g**, Percentage of SNAI1-positive cells in non-EMT and EMT TetON-Snai1 MEOs under different treatment conditions, as indicated. *n* = 20 cells for the Dox−, Dox+ non-EMT and Dox + ML7 non-EMT groups, and *n* = 15 cells for the Dox+ EMT and Dox + ML7 EMT groups. Data represent one of three independent experiments. Unpaired Student's two-tailed *t*-test with Welch's correction. **h**, Immunoblot for SNAI1 and GAPDH from TetON-Snai1 MEOs under different treatment conditions, as indicated. The values indicate the signal intensities of SNAI1 relative to GAPDH. All of the immunofluorescence images and western blots shown represent one of three independent experiments. Scale bars, 25 μm. Error bars represent the s.d. The source data for the graphs can be found in Supplementary Table 3 and unprocessed blots in Supplementary Fig. 7.
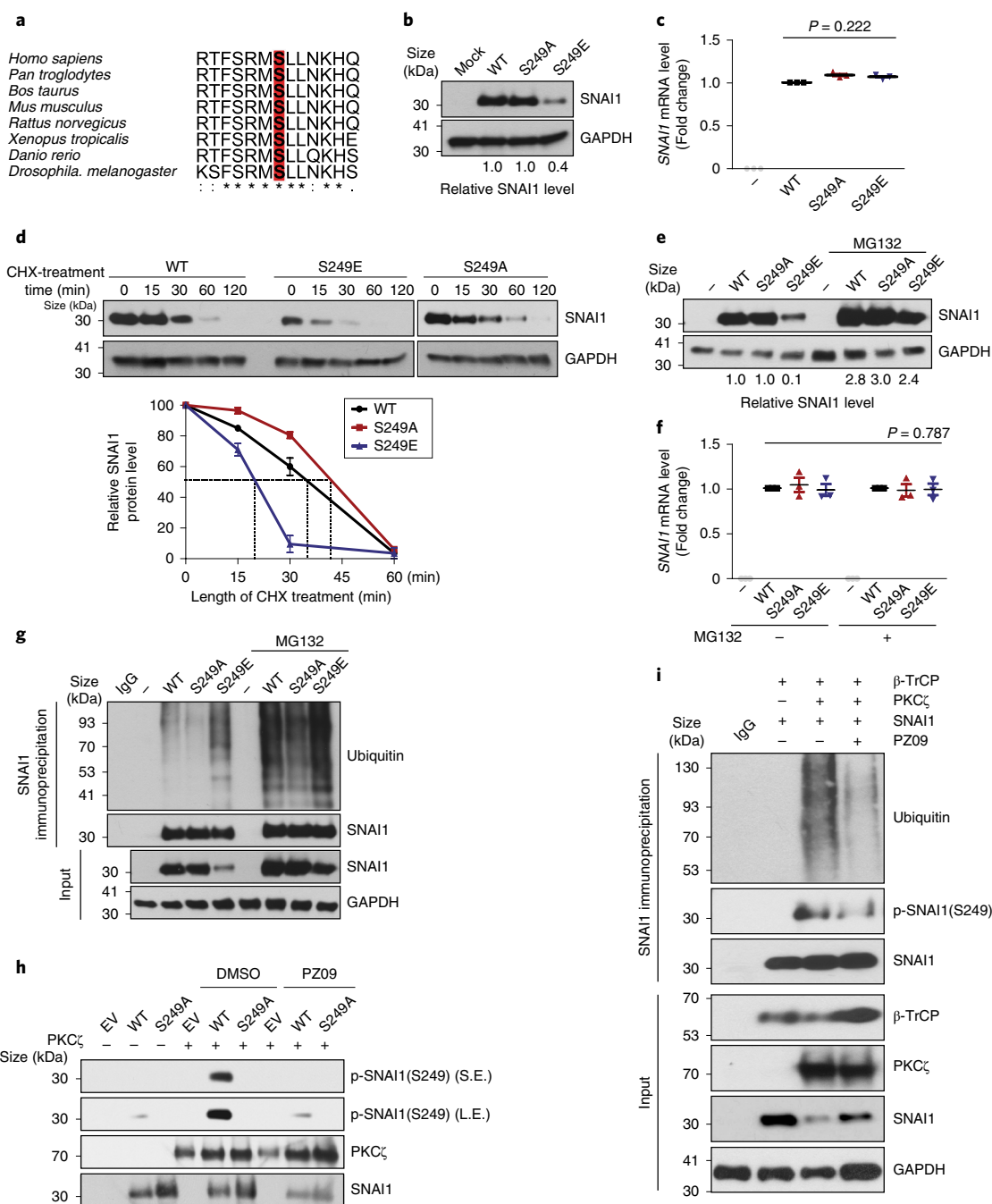
**Fig. 3 | Phosphorylation of S249 on SNAI1 promotes SNAI1 degradation. a**, Alignment of the putative aPKC phosphorylation site in SNAI1 homologs. The alignment was generated by Clustal Omega. *, conserved sequence; :, conservative mutation; ., semi-conservative mutation. **b**, Immunoblot for SNAI1 and GAPDH in MCF10A cells expressing WT, and phospho-deficient S249A and phospho-mimetic S249E mutant SNAI1. The values indicate the signal intensity of SNAI1 relative to GAPDH. $n = 3$ independent experiments. **c**, qPCR analysis of relative *SNAI1* mRNA levels normalized to GAPDH in MCF10A cells expressing WT, and phospho-deficient S249A and phospho-mimetic S249E SNAI1 mutants. Unpaired two-tailed Student's *t*-test with Welch's correction; $n = 3$ independent experiments. **d**, MCF10A cells expressing the indicated SNAI1 constructs were treated with 10 μM cycloheximide for the indicated time points and analysed for SNAI1 and GAPDH by immunoblotting (top). The graph represents the relative SNAI1 proteins levels (bottom). $n = 3$ independent experiments. **e**, MCF10A cells expressing the indicated SNAI1 constructs were treated with 10 μM MG132 for 4 h and the SNAI1 protein levels were analysed by immunoblotting. The values indicate the signal intensities of SNAI1 relative to GAPDH. **f**, qPCR analysis of relative *SNAI1* mRNA levels normalized to GAPDH in MCF10A cells expressing the indicated SNAI1 constructs in the presence of MG132. Paired two-tailed Student's *t*-test; $n = 3$ independent experiments. **g**, SNAI1 proteins were immunoprecipitated from MCF10A cells expressing the indicated SNAI1 constructs with or without MG132 treatment and probed for SNAI1 and ubiquitin. Input, whole cell lysate. **h**, In vitro kinase assay for phospho (p)-SNAI1(S249) with purified WT and S249A SNAI1, and aPKC with or without PZ09 treatment. EV, empty vector. **i**, 293T cells overexpressing SNAI1, aPKC and β-TrCP in the indicated combinations were treated with either 5 μM PZ09 or dimethylsulfoxide (DMSO). SNAI1 proteins were immunoprecipitated from 293T cells and probed for ubiquitin, p-SNAI1(S249), SNAI1 and GAPDH. In **g** and **i**, IgG represents the isotype control. All of the immunofluorescence images and western blots shown represent one of three independent experiments. Error bars represent the s.d. The source data for the graphs can be found in Supplementary Table 3 and unprocessed blots in Supplementary Fig. 7.
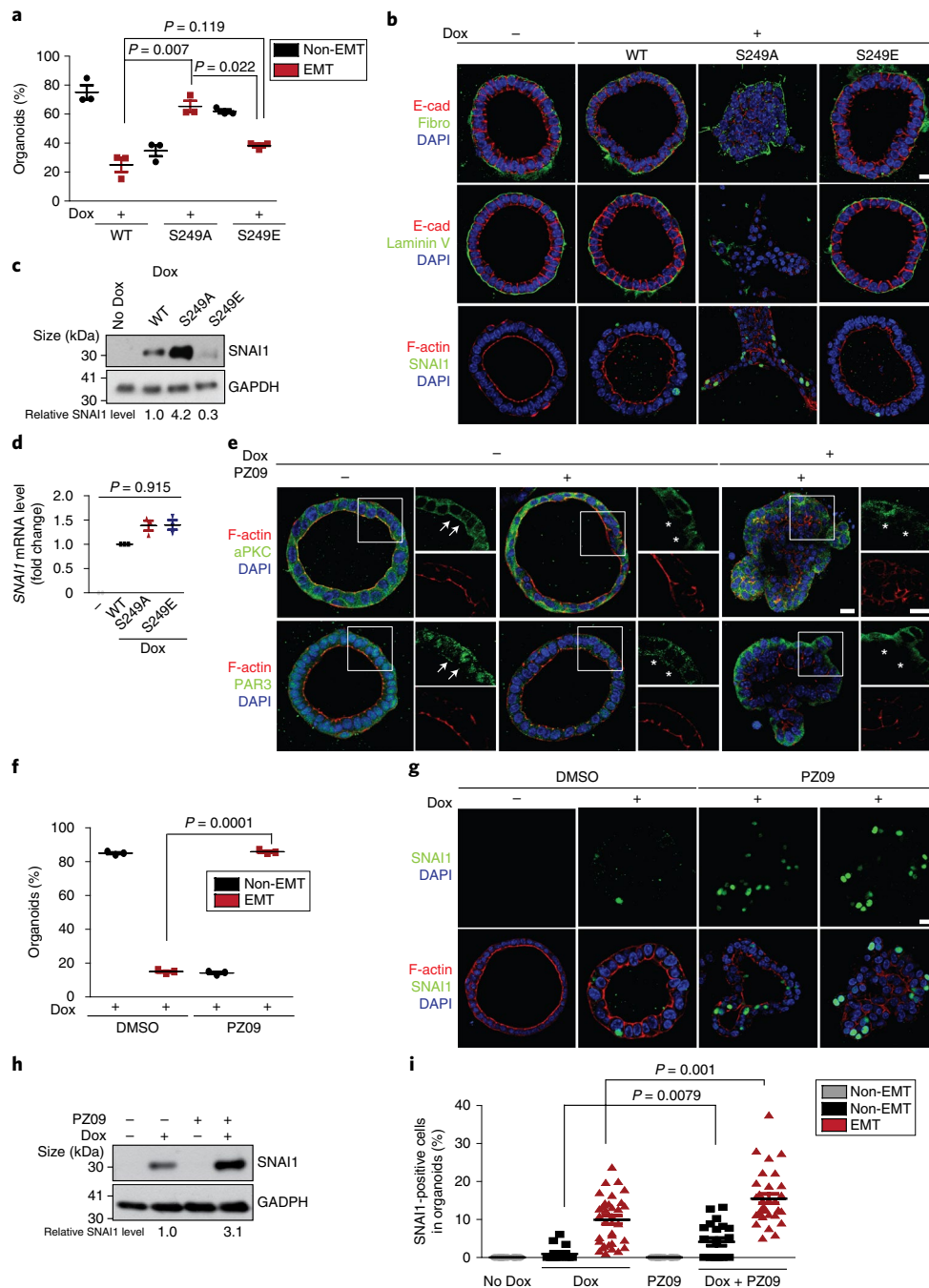
**Fig. 4 | Inhibition of aPKC promotes SNAI1 protein stability and synergizes with SNAI1 induction to promote EMT in MEOs. a**, Quantification of the percentage of non-EMT and EMT MEOs expressing TetON-Snai1 WT and mutants. Unpaired two-tailed Student's $t$-tests with Welch's correction; $n = 3$ independent experiments with 50 organoids per condition in each experiment. **b**, Immunofluorescence images for E-cadherin, fibronectin, laminin V, SNAI1 and F-actin in MEOs expressing TetON-Snai1 WT and mutants. Scale bar, 25 μm. **c**, Immunoblot for SNAI1 and GAPDH in MEOs expressing TetON-Snai1 WT and mutants. The values indicate the SNAI1 signal intensities relative to GAPDH. **d**, qPCR analysis of relative *SNAI1* mRNA levels normalized to GAPDH in MEOs expressing TetON-Snai1 WT and mutants. Unpaired two-tailed Student's $t$-test with Welch's correction. **e**, Immunofluorescence images for aPKC, PAR3 and F-actin in TetON-Snai1 MEOs under different treatment conditions, as indicated. Scale bars, 25 μm and 50 μm. The arrowheads point to the presence of aPKC and F-actin at the apical membrane and PAR3 at the apical–lateral region. The asterisks mark the loss of these proteins at the corresponding areas. **f**, Quantification of the percentage of non-EMT and EMT TetON-Snai1 MEOs in response to PZ09 treatment. Unpaired two-tailed Student's$t$-test with Welch's correction; $n = 3$ independent experiments with 50 organoids per condition in each experiment. **g**, Immunofluorescence images for SNAI1 and F-actin in TetON-Snai1 MEOs in response to PZ09 treatment. Scale bar, 25 μm. **h**, Immunoblot for SNAI1 and GAPDH in TetON-Snai1 MEOs in response to PZ09 treatment. The values indicate the signal intensity of SNAI1 relative to GAPDH. **i**, Quantification of the percentage of SNAI1-positive cells in non-EMT and EMT TetON-Snai1 MEOs in response to PZ09 treatment. $n = 20$ cells for the Dox− and PZ09 groups; $n = 15$, 22 and 32 cells for the Dox+ non-EMT, Dox + PZ09 non-EMT and Dox + PZ09 EMT groups, respectively. Unpaired two-tailed Student's $t$-test with Welch's correction. All of the immunofluorescence images and western blots shown represent one of three independent experiments. Error bars represent the s.d. The source data for the graphs can be found in Supplementary Table 3 and unprocessed blots in Supplementary Fig. 7.
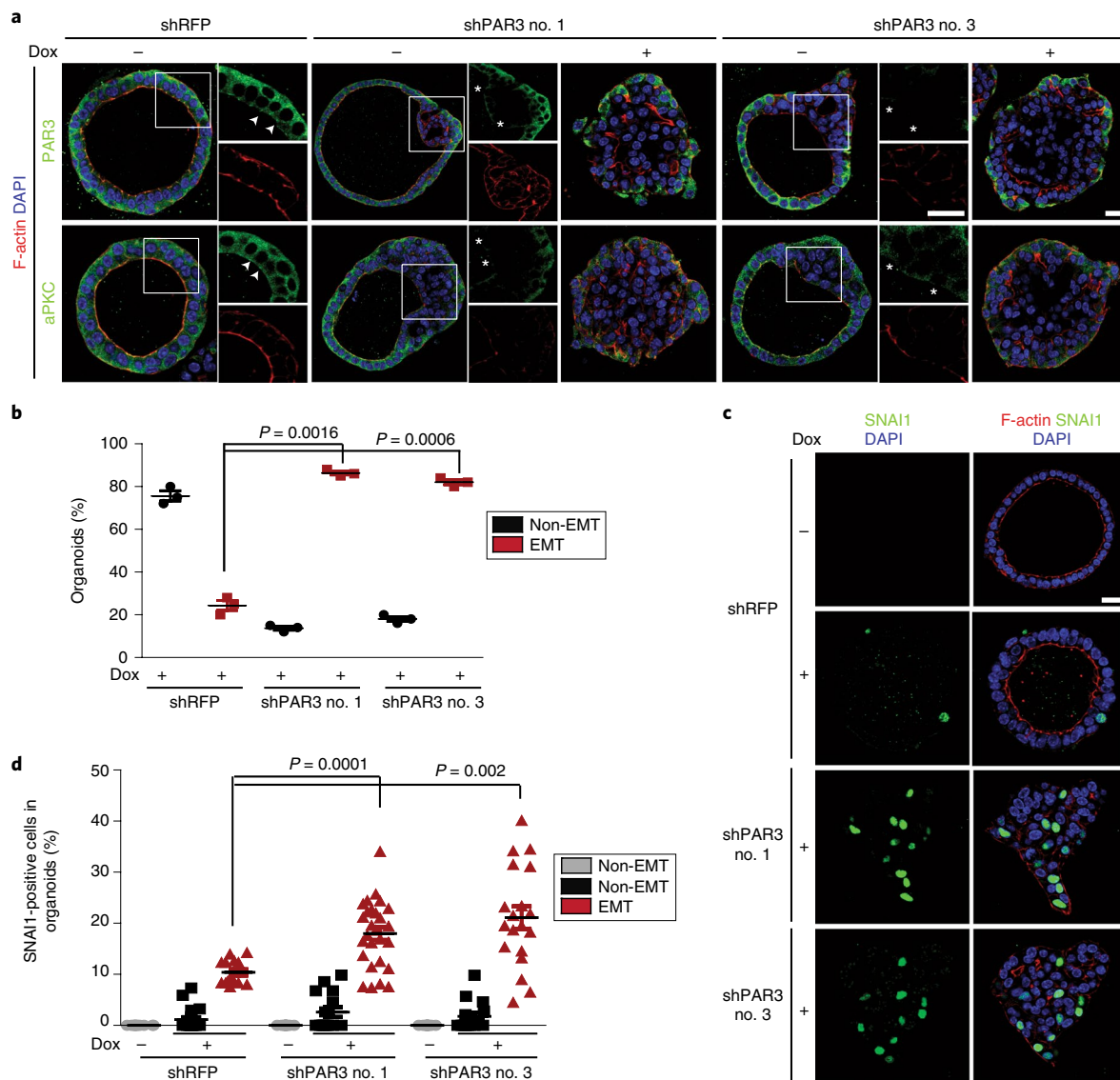
**Fig. 5 | Knockdown of *PAR3* promotes SNAI1 protein stability and induces EMT in MEOs. a**, Representative immunofluorescence images for PAR3, aPKC and F-actin in TetON-Snai1 MEOs expressing control shRFP (shRNA against *RFP* RNA, negative control) or shPAR3 nos 1 and 3 (shRNAs directed against *PAR3*). The arrowheads point to the presence of aPKC at the apical membrane and PAR3 at the apical–lateral region. The asterisks mark the loss of these proteins at the corresponding areas. Scale bars, 25 μm and 50 μm. *n* = 3 independent experiments. **b**, Quantification of the percentage of non-EMT and EMT TetON-Snai1 MEOs expressing shRFP or shPAR3 nos 1 and 3. *n* = 3 independent experiments with 50 organoids per condition in each experiment. **c**, Immunofluorescence images for SNAI1 and F-actin in TetON-Snai1 MEOs expressing shRFP or shPAR3 nos 1 and 3 before and after doxycycline treatment. Scale bar, 25 μm; *n* = 3 independent experiments. **d**, Quantification of the percentage of SNAI1-positive cells in non-EMT and EMT TetON-Snai1 MEOs expressing shRFP or shPAR3 nos 1 and 3 before and after doxycycline treatment. *n* = 20, 20, 15, 20, 15, 27, 20, 15 and 19 cells for the groups in the graph, listed from left to right. The data represent one of three independent experiments. Error bars represent the s.d. Unpaired two-tailed Student's *t*-tests with Welch's correction. All of the immunofluorescence images represent one of three independent experiments. The source data for the graphs can be found in Supplementary Table 3.

levels (Fig. 4h). Treatment of MEOs with PZ09 consistently resulted in a significant increase in the percentage of SNAI1-positive cells in individual organoids (Fig. 4g–i). Our results suggest that aPKC kinase activity is required for SNAI1 phosphorylation and degradation in polarized MEOs.

We next expressed short hairpin RNAs (shRNA) against *PAR3* by lentiviral infection of primary MEOs isolated from the TetON-Snai1 mice. Partial knockdown of *PAR3* caused the loss of apical–basal polarity in certain areas of MEOs and mislocalization of PKCζ from the apical area (Fig. 5a). Functionally, knockdown of *PAR3* synergized with the induction of SNAI1 to promote EMT in MEOs (Fig. 5b).

Importantly, knockdown of *PAR3* increased the percentage of SNAI1-positive cells in individual MEOs (Fig. 5c,d). Together, these data demonstrate that the PAR complex is required for aPKC-regulated SNAI1 destabilization to prevent EMT in polarized MEOs.

**The PAR3–aPKC complex destabilizes endogenous SNAI1 protein to prevent EMT.** We next investigated endogenous human SNAI1 regulation by polarity using Caco2 human intestinal epithelial cells that express endogenous *SNAI1* mRNA and develop well-established apical–basal polarity in 3D (ref. [37]). The endogenous SNAI1 protein level was consistently and significantly reduced in
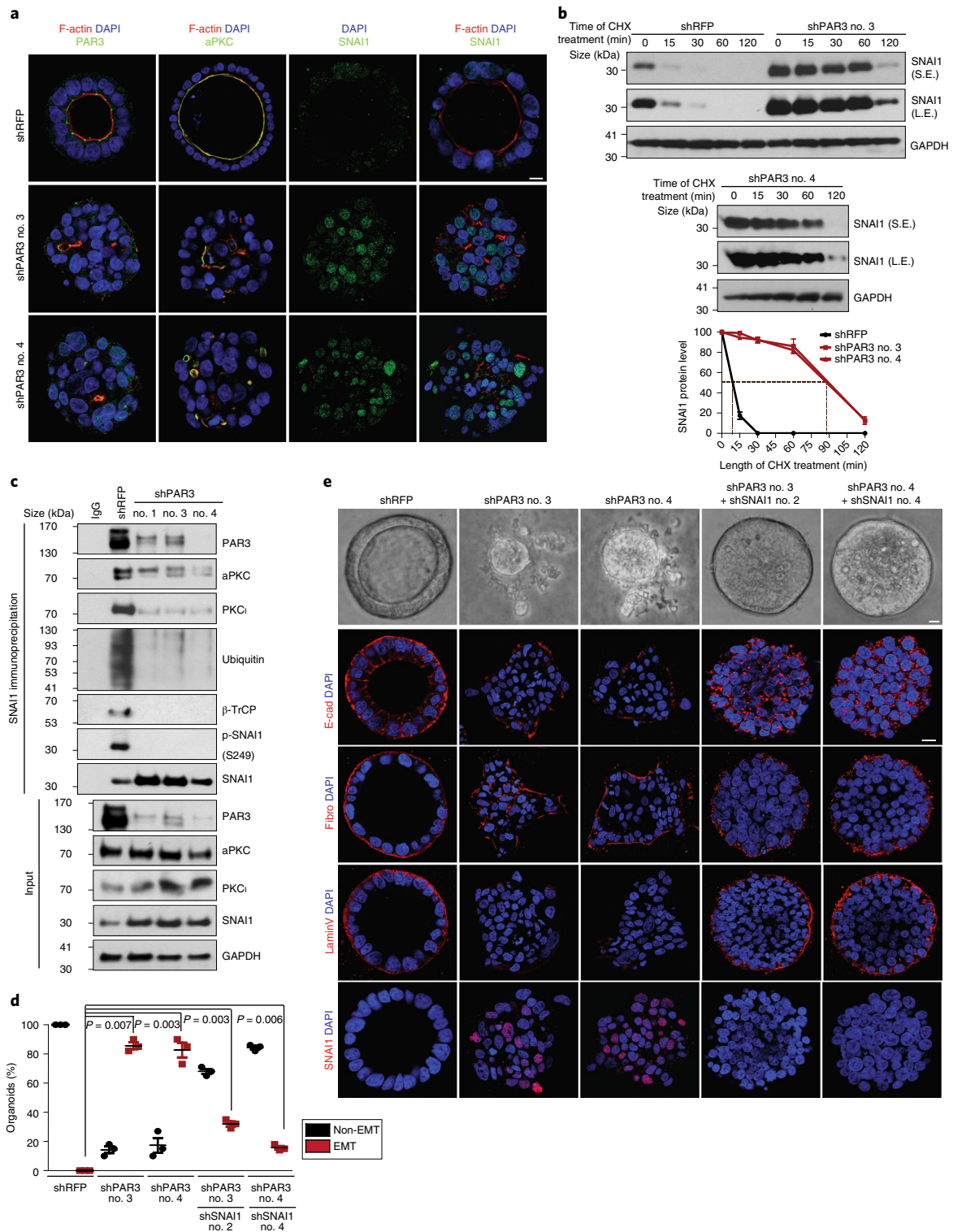
**Fig. 6 | Loss of PAR3 stabilizes endogenous SNAI1 protein and induced EMT in 3D Caco2 organoids. a**, Immunofluorescence images for PAR3, aPKC, SNAI1 and F-actin in Caco2 organoids expressing shRFP or shPAR3 nos 3 and 4. **b**, Caco2 organoids expressing shRFP and shPAR3 nos 3 and 4 were treated with 10 μM cycloheximide for the indicated time periods and analysed for SNAI1 and GAPDH by immunoblotting (top). The graph represents the quantification of SNAI1 protein levels relative to GAPDH (bottom). $n = 3$ independent experiments. **c**, Endogenous SNAI1 proteins were immunoprecipitated from Caco2 organoids expressing shRFP or shPAR3 nos 1, 3 and 4 and probed for PAR3, aPKC, PKCι, ubiquitin, β-TrCP, p-SNAI1(S249) and SNAI1 (top). Immunoblot for PAR3, aPKC, PKCι, SNAI1 and GAPDH in Caco2 organoids expressing shRFP or shPAR3 nos 1, 3 and 4 (bottom). **d**, Quantification of the percentage of non-EMT and EMT TetON-Snai1 MEOs expressing the indicated shRNA constructs. shSNAI1 nos 2 and 4 represent different shRNAs targeting SNAI1. Data from three independent experiments are represented; $n = 50$ organoids per condition in each experiment; paired two-tailed $t$-tests. **e**, Representative bright-field (top) and immunofluorescence (bottom) images for GFP, E-cadherin, fibronectin, laminin V and SNAI1 (bottom) of Caco2 organoids expressing the indicated shRNA constructs. Scale bars, 25 μm. Error bars represent the s.d.
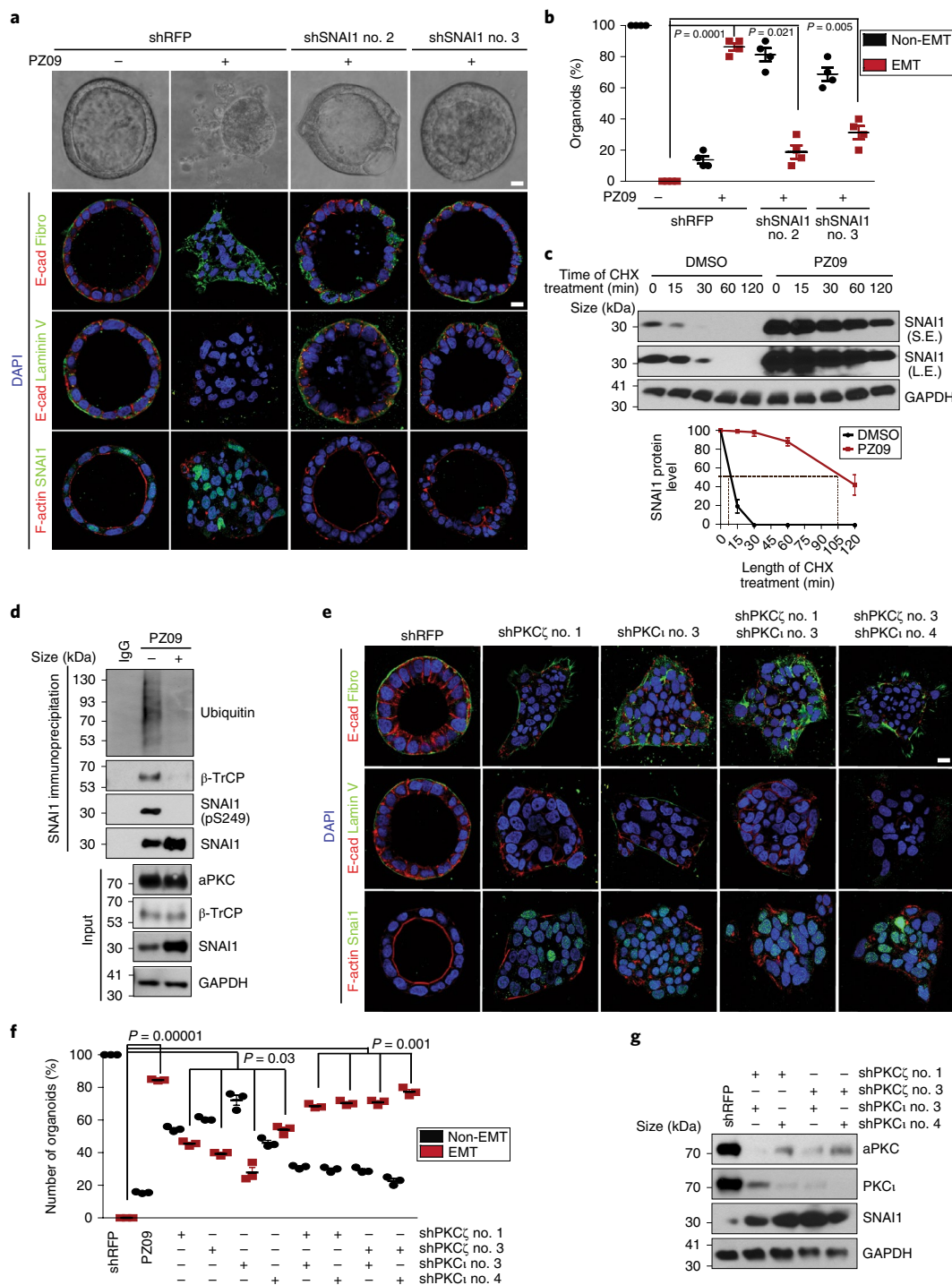
**Fig. 7 | Suppression of aPKCs increases endogenous SNAI1 stability and promotes EMT in 3D Caco2 organoids. a**, Representative immunofluorescence images for E-cadherin, fibronectin, laminin V, SNAI1 and F-actin in Caco2 organoids expressing shRFP or shSNAI1 nos 2 and 3 with or without PZ09 treatment. $n=3$ independent experiments. **b**, Quantification of the percentage of non-EMT and EMT Caco2 organoids expressing shRFP or shSNAI1 nos 2 and 3 with or without PZ09 treatment. $n=3$ independent experiments with 50 organoids per condition in each experiment; paired two-tailed Student's $t$-tests. **c**, Caco2 organoids were treated with either DMSO or PZ09, followed by $10\,\mu M$ cycloheximide for the indicated time periods and analysed for SNAI1 and GAPDH by immunoblotting (top). The graph represents the quantification of SNAI1 proteins levels relative to GAPDH (bottom). $n=3$ independent experiments. **d**, Endogenous SNAI1 proteins were immunoprecipitated from Caco2 organoids with or without PZ09 treatment and probed for ubiquitin, β-TrCP, p-SNAI1(S249) and SNAI1 (top). Immunoblot for aPKC, β-TrCP, SNAI1 and GAPDH in Caco2 organoids with or without PZ09 treatment (bottom). **e**, Representative immunofluorescence images for E-cadherin, fibronectin, laminin V, SNAI1 and F-actin in Caco2 organoids expressing the indicated shRNA constructs. shPKCζ and shPKCι constructs represent shRNAs targeting PKCζ and PKCι isoforms, respectively. **f**, Quantification of the percentage of non-EMT and EMT Caco2 organoids expressing the indicated shRNA constructs. $n=3$ independent experiments with 50 organoids per condition in each experiment; paired two-tailed Student's $t$-tests. **g**, Immunoblot for aPKC, PKCι, SNAI1 and GAPDH in lysates from Caco2 organoids expressing the indicated shRNA constructs. All of the immunofluorescence images and western blots shown represent one of three independent experiments. Scale bars, $25\,\mu m$. Error bars represent the s.d. The source data for the graphs can be found in Supplementary Table 3 and unprocessed blots in Supplementary Fig. 7.
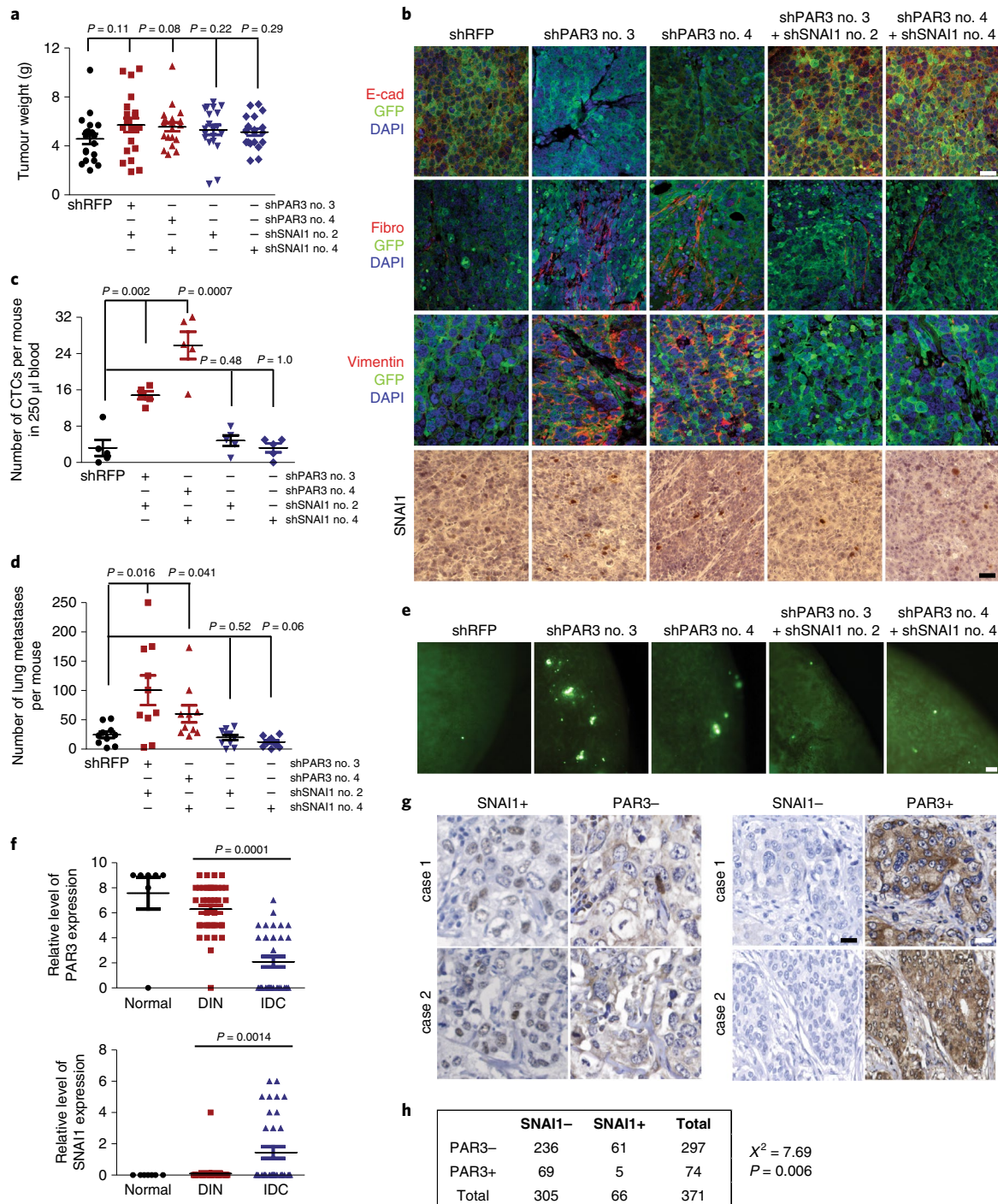
**Fig. 8 | The epithelial-polarity-regulated SNAI1 degradation mechanism impacts tumour invasion and metastasis in vivo and is associated with human breast cancer progression. a,** Primary tumour weight of GFP-tagged Caco2 xenograft tumours expressing shRFP, shPAR3 and a combination of shPAR3 and shSNAI1 after subcutaneous injection for six weeks. Unpaired two-tailed Student's $t$-tests with Welch's correction; $n = 20$ tumours per group. **b,** Immunofluorescence images for GFP, E-cadherin and human vimentin (top), and immunohistochemistry images for SNAI1 in Caco2 xenograft tumours expressing shRFP, shPAR3 and shPAR3-shSNAI1 (bottom). Scale bars, 50 μm for SNAI1 staining and 25 μm for all other markers. **c,** Quantification of the number of circulating tumour cells (CTCs) isolated from mice carrying Caco2 tumours that express shRFP, shPAR3 and shPAR3-shSNAI1. Unpaired two-tailed Student's $t$-tests with Welch's correction; $n = 10$ mice per group. **d,** Quantification of GFP-positive metastatic events in the lung of mice carrying Caco2 tumours expressing shRFP, shPAR3 and shPAR3-shSNAI1. Unpaired two-tailed Student's $t$-tests with Welch's correction; $n = 10$ mice per group. **e,** Fluorescent images of GFP-positive metastatic lesions in the lung of mice carrying Caco2 tumours expressing shRFP, shPAR3 and shPAR3-shSNAI1. The GFP signal indicates disseminated tumour cells in the lung. Scale bar, 100 μm. **f,** Quantification of the relative PAR3 and SNAI1 signals in human breast tumour tissue samples ($n = 48$ patients; two sections from each patient were analysed). Unpaired two-tailed Student's $t$-test with Welch's correction. **g,** Representative immunohistochemistry images for SNAI1 and PAR3 in human breast tumour samples. Scale bars, 25 μm. **h,** Correlation analysis of SNAI1 and PAR3 in human Stage 2 breast tumour TMA (table shows number of tumours from the tissue microarray). DIN, ductal intraepithelial neoplasia; IDC, invasive ductal carcinoma. Error bars represent the s.d. All of the data panels represent one of three independent experiments. The source data for the graphs can be found in Supplementary Table 3.

3D polarized organoids compared with sparse 2D cultures without polarity. Immunoprecipitated endogenous SNAI1 protein is specifically phosphorylated at S249, is ubiquitinated and interacts with β-TrCP only in polarized 3D organoids, but not in 2D cultures (Supplementary Fig. 4a). PAR3 and aPKC proteins were specifically localized at the apical membrane in control organoids, whereas knockdown of *PAR3* completely disrupted apical–basal polarity and caused mislocalization of aPKCs (Fig. 6a). In control organoids, SNAI1 protein was largely undetectable; following knockdown of *PAR3*, most cells in individual organoids became positive for endogenous SNAI1 protein (Fig. 6a). SNAI1 protein rapidly degraded with a half-life of <10 min in control organoids, whereas *PAR3* knockdown elongated the half-life of SNAI1 to more than 80 min (Fig. 6b). *PAR3* knockdown consistently increased endogenous SNAI1 levels without affecting *SNAI1* mRNA levels (Fig. 6c and Supplementary Fig. 4b). SNAI1 immunoprecipitated from Caco2 organoids is phosphorylated on S249 and interacts with both PAR3 and β-TrCP. Interestingly, both aPKC members (PKCζ and PKCι) are associated with SNAI1 in the control organoids. Importantly, knockdown of *PAR3* abolished S249 phosphorylation on SNAI1 and significantly reduced the interaction between SNAI1 and aPKCs or β-TrCP (Fig. 6c). Consequently, more than 80% of the organoids in 3D culture underwent EMT following knockdown of *PAR3*, as immunostaining showed reduced E-cadherin-mediated junctions, loss of laminin V and increased fibronectin expression (Fig. 6d,e). Importantly, PAR3 loss-induced EMT and invasion through the basement membrane could be significantly blocked following the deletion of *SNAI1* despite polarity loss caused by *PAR3* knockdown (Fig. 6d,e and Supplementary Fig. 4c). These data strongly support a critical role of the PAR complex in reducing endogenous SNAI1 protein stability and blocking SNAI1-induced EMT.

We next investigated whether inactivation of aPKCs affects endogenous SNAI1 phosphorylation of S249 and subsequent degradation in Caco2 3D organoids. PZ09 effectively inhibited the aPKC kinase activity in Caco2 3D organoids, as assessed using an aPKC-specific fluorescence resonance energy transfer reporter[38] (Supplementary Fig. 5a). Morphologically, following PZ09 treatment, more than 90% of the Caco2 organoids lost apical–basal polarity, E-cadherin-mediated adherens junctions, basement membrane integrity and increased fibronectin expression, which is consistent with increases of SNAI1-positive cells (Fig. 7a,b and Supplementary Fig. 5c). Inhibition of aPKC kinase activity also increased SNAI1 protein levels and led to the expression of SNAI1 by the majority of cells in individual organoids without affecting *SNAI1* mRNA levels (Supplementary Fig. 5b–d). The half-life of SNAI1 protein was increased from <10 min to >100 min following inhibition of aPKCs (Fig. 7c). Notably, we found that endogenous SNAI1 protein is phosphorylated at S249, ubiquitinated, interacts with β-TrCP and all of these events were inhibited by PZ09 treatment (Fig. 7d). We next investigated whether endogenous SNAI1 protein is required for the induction of EMT following aPKC inhibition in Caco2 organoids. Knockdown of *SNAI1* significantly blocked EMT induction in response to PZ09 treatment (Fig. 7a,b and Supplementary Fig. 5d), suggesting that inhibition of aPKC kinase activity promotes EMT in a SNAI1-dependent manner.

We next examined the individual contributions of PKCζ and PKCι. Although single knockdown of PKCζ or PKCι could partially stabilize SNAI1 and promote EMT in some organoids, only double knockdown of both PKCζ and PKCι could fully recapitulate the EMT and invasion phenotype induced by PZ09 treatment (Fig. 7e–g and Supplementary Fig. 5e,f), which suggests that PKCζ and PKCι have redundant roles in the PAR complex to phosphorylate SNAI1 at S249. These data strongly indicate that both aPKC members in the PAR complex are responsible for the S249 phosphorylation of endogenous SNAI1 protein and subsequent ubiquitination and degradation of the SNAI1 protein. Together, these findings

demonstrate that apical–basal polarity promotes endogenous SNAI1 protein phosphorylation and degradation via active aPKCs in the PAR complex to prevent EMT.

**Loss of the PAR-complex-mediated polarity promotes invasion and metastasis via SNAI1 in vivo.** We implanted GFP-labelled Caco2 cells expressing control shRNA, shRNAs against *PAR3* and shRNAs against *PAR3* and *SNAI1* in mice to follow the development and metastasis of primary tumours. Control Caco2 cells developed primary tumours that presented an epithelial morphology. In contrast, the loss of PAR3 resulted in mesenchymal primary tumours with very low membranous E-cadherin, high human vimentin and high SNAI1 expression. More importantly, knockdown of SNAI1 reversed the mesenchymal phenotype in Caco2 tumours expressing shRNAs against *PAR3* (Fig. 8a,b and Supplementary Fig. 6a). Consistent with the results in Fig. 6, Caco2 control tumours were largely negative for SNAI1 immunostaining, whereas the knockdown of *PAR3* increased SNAI1 protein expression (Fig. 8b). Moreover, mice carrying *PAR3*-knockdown tumours presented significantly more circulating tumour cells compared with mice carrying the control Caco2 tumours and the knockdown of *SNAI1* significantly reduced circulating tumour cell numbers to that of the control (Fig. 8c). Furthermore, we observed a significant increase in GFP-positive disseminated tumour cells in the lungs of mice carrying *PAR3*-knockdown tumours compared with controls and this increase in lung dissemination was completely blocked by SNAI1 knockdown (Fig. 8d,e). These in vivo results strongly support our cellular and biochemical data showing that the PAR-complex-mediated SNAI1 protein degradation inhibits EMT, tumour invasion and metastasis in vivo.

**PAR3 and SNAI1 expression are negatively correlated in human breast tissue samples.** We next evaluated the involvement of the PAR3–SNAI1 regulatory mechanism in human breast cancer initiation and progression by immunostaining analysis for PAR3 and SNAI1 expression in human breast tissue microarray (TMA). PAR3 protein was detected at the apical membrane in normal mammary ducts and in the majority of ductal intraepithelial neoplasia samples, whereas expression of these proteins was clearly decreased in invasive ductal carcinoma samples. The reverse was observed for SNAI1, where SNAI1 protein was largely undetectable in normal and ductal intraepithelial neoplasia samples and was only evident in invasive ductal carcinoma samples (Fig. 8f and Supplementary Fig. 6b). We next analysed PAR3 and SNAI1 expression in a cohort of 371 Stage 2 breast tumours from the NCI Cancer Diagnosis Program. Consistent with a suppressive function of the PAR epithelial polarity complexes on SNAI1 stability, 92% of the SNAI1-positive tumours were negative for PAR3 (Fig. 8g,h). It is important to note that SNAI1 expression is regulated at the transcriptional and post-translational levels. This is consistent with Fig. 8h, which shows that among the 297 PAR3-negative tumours, 61 were positive for SNAI1, whereas the remaining 80% were still negative for SNAI1, possibly due to the lack of *SNAI1* mRNA expression. Our results suggest that the molecular machinery that links the PAR3 complex with SNAI1 protein stability may also contribute to human breast tumour progression.

## Discussion

We demonstrate that apical–basal polarity directly impinges on the EMT program to prevent EMT and invasion, thus inhibiting metastasis. Mechanistically, we show that under intact polarity, active aPKCs in the PAR complex phosphorylate SNAI1 at S249, which in turn promotes ubiquitination and degradation of the SNAI1 protein. Inactivation of the PAR3–aPKC polarity machinery stabilizes SNAI1 protein, thus promoting SNAI1-induced EMT and invasion. In vivo, the aPKC-mediated phosphorylation of SNAI1 hampers

the ability of SNAI1 to promote breast tumour cells to invade, disseminate and metastasize to distant organs. The downregulation of PAR3 and increase in SNAI1 protein expression are associated with breast tumour progression in human breast cancer patients. Our findings reveal a direct molecular link between apical–basal polarity and the core EMT transcription machinery in tumour invasion and metastasis (Supplementary Fig. 6c).

Previous studies of EMT regulation of epithelial cell properties focused on cell–cell junctions, such as tight junctions and adherens junctions[22]. Although loss of cell polarity is an early step during the EMT process, polarity is largely thought to be a passive recipient of the EMT-inducing signals to decrease epithelial characteristics. The results from this study show that apical–basal polarity actively inhibits the core EMT transcriptional program by destabilizing the SNAI1 protein. Given the key role of SNAI1 in suppressing proteins that are associated with cell–cell junctions[33,39], our results introduce the concept that apical–basal polarity is actively involved in maintaining epithelial cell–cell junctions by suppressing the EMT program. Importantly, our study also demonstrates that polarity is a critical checkpoint during EMT. A number of key EMT transcription factors, particularly SNAI1 and ZEB1, have been shown to suppress transcription of several key polarity genes, including *Crb3*, *PATj* and *LGL2*, thus disrupting apical–basal polarity[22,40–42]. Consequently, the loss of epithelial polarity sends a positive feedback signal to further stabilize SNAI1 and move the EMT process forwards to promote tumour progression (Supplementary Fig. 6c). The majority of human carcinomas show a loss of apical–basal polarity during the progression from intraepithelial neoplasia to invasive carcinoma[43–45]. Our work (and several previous studies) links epithelial cell polarity proteins, such as PAR3 and aPKCs, to metastasis suppression[2]. The loss of PAR3 promotes cancer metastasis through the activation of Tiam1-mediated Rac-GTP pathway and inhibition of E-cadherin junction stability[12]. In addition, loss of PAR3 accelerates breast cancer formation and metastasis through aPKC-mediated Jak–Stat3 signalling[10]. This study adds SNAI1 as a key target of the PAR–aPKC polarity complex in suppressing tumour invasion and metastasis. Together, these findings support the idea that epithelial cell polarity proteins function as major metastasis suppressors through several pathways to maintain epithelial characteristics in carcinomas.

SNAI1 stability is also regulated by phosphorylation of the SNAI1 protein by GSK3β[33,34]. Our study shows that inhibiting GSK3 under both polarized and unpolarized conditions stabilized the SNAI1 protein to the same degree. These data show that GSK3 inhibition cannot rescue polarity-mediated SNAI1 degradation and that GSK3 promotes SNAI1 degradation regardless of the polarity status. SNAI1 could therefore be regulated by diverse upstream signals independently to regulate its stability to impact EMT.

Our data identify an unexpected role for aPKCs in suppressing EMT, thus inhibiting tumour invasion and metastasis. Previous studies suggest that aPKCs may promote tumour proliferation and progression[10,46–49]. However, these studies were largely performed in cells that lack apical–basal polarity and may thus reflect polarity-independent functions of aPKCs. For example, in addition to their function in the PAR complex, aPKCs also bind to another scaffold protein p62 to function in response to tumour necrosis factor α, lipopolysaccharide and interleukin-1 (ref. [50]). It is therefore critical to analyse aPKCs under specific physiological conditions to reveal the diverse roles of this unique PKC subfamily in tumour progression and metastasis.

## Online content

Any methods, additional references, Nature Research reporting summaries, source data, statements of data availability and associated accession codes are available at https://doi.org/10.1038/s41556-019-0291-8.

## References

1. Royer, C. & Lu, X. Epithelial cell polarity: a major gatekeeper against cancer? *Cell Death Differ.* **18**, 1470–1477 (2011).
2. Zen, K. et al. Defective expression of polarity protein PAR-3 gene (*PARD3*) in esophageal squamous cell carcinoma. *Oncogene* **28**, 2910–2918 (2009).
3. Assemat, E., Bazellieres, E., Pallesi-Pocachard, E., Le Bivic, A. & Massey-Harroche, D. Polarity complex proteins. *Biochim. Biophys. Acta* **1778**, 614–630 (2008).
4. Lee, M. & Vasioukhin, V. Cell polarity and cancer—cell and tissue polarity as a non-canonical tumor suppressor. *J. Cell Sci.* **121**, 1141–1150 (2008).
5. Ngok, S. P., Lin, W. H. & Anastasiadis, P. Z. Establishment of epithelial polarity—GEF who's minding the GAP? *J. Cell Sci.* **127**, 3205–3215 (2014).
6. Horikoshi, Y. et al. Interaction between PAR-3 and the aPKC–PAR-6 complex is indispensable for apical domain development of epithelial cells. *J. Cell Sci.* **122**, 1595–1606 (2009).
7. Goldstein, B. & Macara, I. G. The PAR proteins: fundamental players in animal cell polarization. *Dev. Cell* **13**, 609–622 (2007).
8. Nagai-Tamai, Y., Mizuno, K., Hirose, T., Suzuki, A. & Ohno, S. Regulated protein–protein interaction between aPKC and PAR-3 plays an essential role in the polarization of epithelial cells. *Genes Cells* **7**, 1161–1171 (2002).
9. Graybill, C., Wee, B., Atwood, S. X. & Prehoda, K. E. Partitioning-defective protein 6 (Par-6) activates atypical protein kinase C (aPKC) by pseudosubstrate displacement. *J. Biol. Chem.* **287**, 21003–21011 (2012).
10. McCaffrey, L. M., Montalbano, J., Mihai, C. & Macara, I. G. Loss of the Par3 polarity protein promotes breast tumorigenesis and metastasis. *Cancer Cell* **22**, 601–614 (2012).
11. McCaffrey, L. M. & Macara, I. G. Signaling pathways in cell polarity. *Cold Spring Harb. Perspect. Biol.* **4**, a009654 (2012).
12. Xue, B., Krishnamurthy, K., Allred, D. C. & Muthuswamy, S. K. Loss of Par3 promotes breast cancer metastasis by compromising cell–cell cohesion. *Nat. Cell Biol.* **15**, 189–200 (2013).
13. Iden, S. et al. Tumor type-dependent function of the Par3 polarity protein in skin tumorigenesis. *Cancer Cell* **22**, 389–403 (2012).
14. Brabletz, T. To differentiate or not—routes towards metastasis. *Nat. Rev. Cancer* **12**, 425–436 (2012).
15. Tsai, J. H. & Yang, J. Epithelial–mesenchymal plasticity in carcinoma metastasis. *Genes Dev.* **27**, 2192–2206 (2013).
16. Nieto, M. A., Huang, R. Y., Jackson, R. A. & Thiery, J. P. EMT: 2016. *Cell* **166**, 21–45 (2016).
17. Kalluri, R. & Weinberg, R. A. The basics of epithelial–mesenchymal transition. *J. Clin. Invest.* **119**, 1420–1428 (2009).
18. Lamouille, S., Xu, J. & Derynck, R. Molecular mechanisms of epithelial–mesenchymal transition. *Nat. Rev. Mol. Cell Biol.* **15**, 178–196 (2014).
19. De Craene, B. & Berx, G. Regulatory networks defining EMT during cancer initiation and progression. *Nat. Rev. Cancer* **13**, 97–110 (2013).
20. Yang, J. & Weinberg, R. A. Epithelial–mesenchymal transition: at the crossroads of development and tumor metastasis. *Dev. Cell* **14**, 818–829 (2008).
21. Barrallo-Gimeno, A. & Nieto, M. A. The *Snail* genes as inducers of cell movement and survival: implications in development and cancer. *Development* **132**, 3151–3161 (2005).
22. Moreno-Bueno, G., Portillo, F. & Cano, A. Transcriptional regulation of cell polarity in EMT and cancer. *Oncogene* **27**, 6958–6969 (2008).
23. de Herreros, A. G., Peiro, S., Nassour, M. & Savagner, P. Snail family regulation and epithelial mesenchymal transitions in breast cancer progression. *J. Mammary Gland Biol. Neoplas.* **15**, 135–147 (2010).
24. Ocana, O. H. et al. Metastatic colonization requires the repression of the epithelial–mesenchymal transition inducer Prrx1. *Cancer Cell* **22**, 709–724 (2012).
25. Tsai, J. H., Donaher, J. L., Murphy, D. A., Chau, S. & Yang, J. Spatiotemporal regulation of epithelial–mesenchymal transition is essential for squamous cell carcinoma metastasis. *Cancer Cell* **22**, 725–736 (2012).
26. Tran, H. D. et al. Transient SNAIL1 expression is necessary for metastatic competence in breast cancer. *Cancer Res.* **74**, 6330–6340 (2014).
27. Jung, H. Y., Fattet, L. & Yang, J. Molecular pathways: linking tumor microenvironment to epithelial–mesenchymal transition in metastasis. *Clin. Cancer Res.* **21**, 962–968 (2015).
28. Wei, S. C. et al. Matrix stiffness drives epithelial–mesenchymal transition and tumour metastasis through a TWIST1–G3BP2 mechanotransduction pathway. *Nat. Cell Biol.* **17**, 678–688 (2015).
29. Ewald, A. J. Isolation of mouse mammary organoids for long-term time-lapse imaging. *Cold Spring Harb. Protoc.* **2013**, 130–133 (2013).
30. Shamir, E. R. et al. Twist1-induced dissemination preserves epithelial identity and requires E-cadherin. *J. Cell. Biol.* **204**, 839–856 (2014).

31. Ewald, A. J., Brenot, A., Duong, M., Chan, B. S. & Werb, Z. Collective epithelial migration and cell rearrangements drive mammary branching morphogenesis. *Dev. Cell* **14**, 570–581 (2008).

32. Lou, S. S., Diz-Munoz, A., Weiner, O. D., Fletcher, D. A. & Theriot, J. A. Myosin light chain kinase regulates cell polarization independently of membrane tension or Rho kinase. *J. Cell Biol.* **209**, 275–288 (2015).

33. Peinado, H., Olmeda, D. & Cano, A. Snail, Zeb and bHLH factors in tumour progression: an alliance against the epithelial phenotype? *Nat. Rev. Cancer* **7**, 415–428 (2007).

34. Zhou, B. P. et al. Dual regulation of Snail by GSK-3β-mediated phosphorylation in control of epithelial–mesenchymal transition. *Nat. Cell Biol.* **6**, 931–940 (2004).

35. Joberty, G., Petersen, C., Gao, L. & Macara, I. G. The cell-polarity protein Par6 links Par3 and atypical protein kinase C to Cdc42. *Nat. Cell Biol.* **2**, 531–539 (2000).

36. Tobias, I. S. et al. Protein kinase Cζ exhibits constitutive phosphorylation and phosphatidylinositol-3,4,5-triphosphate-independent regulation. *Biochem. J.* **473**, 509–523 (2016).

37. Durgan, J., Kaji, N., Jin, D. & Hall, A. Par6B and atypical PKC regulate mitotic spindle orientation during epithelial morphogenesis. *J. Biol. Chem.* **286**, 12461–12474 (2011).

38. Tobias, I. S. & Newton, A. C. Protein scaffolds control localized protein kinase Cζ activity. *J. Biol. Chem.* **291**, 13809–13822 (2016).

39. Martinez-Estrada, O. M. et al. The transcription factors Slug and Snail act as repressors of Claudin-1 expression in epithelial cells. *Biochem. J.* **394**, 449–457 (2006).

40. Aigner, K. et al. The transcription factor ZEB1 (δEF1) promotes tumour cell dedifferentiation by repressing master regulators of epithelial polarity. *Oncogene* **26**, 6979–6988 (2007).

41. Spaderna, S. et al. The transcriptional repressor ZEB1 promotes metastasis and loss of cell polarity in cancer. *Cancer Res.* **68**, 537–544 (2008).

42. Whiteman, E. L., Liu, C. J., Fearon, E. R. & Margolis, B. The transcription factor snail represses *Crumbs3* expression and disrupts apico-basal polarity complexes. *Oncogene* **27**, 3875–3879 (2008).

43. Rothenberg, S. M. et al. A genome-wide screen for microdeletions reveals disruption of polarity complex genes in diverse human cancers. *Cancer Res.* **70**, 2158–2164 (2010).

44. Chatterjee, S. J. & McCaffrey, L. Emerging role of cell polarity proteins in breast cancer progression and metastasis. *Breast Cancer* **6**, 15–27 (2014).

45. Muthuswamy, S. K. & Xue, B. Cell polarity as a regulator of cancer cell behavior plasticity. *Annu. Rev. Cell Dev. Biol.* **28**, 599–625 (2012).

46. Parker, P. J., Justilien, V., Riou, P., Linch, M. & Fields, A. P. Atypical protein kinase Cι as a human oncogene and therapeutic target. *Biochem. Pharmacol.* **88**, 1–11 (2014).

47. Gunaratne, A., Thai, B. L. & Di Guglielmo, G. M. Atypical protein kinase C phosphorylates Par6 and facilitates transforming growth factor β-induced epithelial-to-mesenchymal transition. *Mol. Cell. Biol.* **33**, 874–886 (2013).

48. Guyer, R. A. & Macara, I. G. Loss of the polarity protein PAR3 activates STAT3 signaling via an atypical protein kinase C (aPKC)/NF-κB/interleukin-6 (IL-6) axis in mouse mammary cells. *J. Biol. Chem.* **290**, 8457–8468 (2015).

49. Rosse, C. et al. Control of MT1-MMP transport by atypical PKC during breast-cancer progression. *Proc. Natl Acad. Sci. USA* **111**, E1872–E1879 (2014).

50. Diaz-Meco, M. T. & Moscat, J. The atypical PKCs in inflammation: NF-κB and beyond. *Immunol. Rev.* **246**, 154–167 (2012).

## Acknowledgements

## Author contributions

H.-Y.J., J.H.T and J.Y. conceived the project and designed the experiments. H.-Y.J. performed most of the experiments and made the figures. L.F., J.H.T., T.K. and Q.C. contributed to the experimental work. L.F., J.H.T. and A.C.N. provided advice on experimental design and revised the manuscript. H.J. and J.Y. wrote the manuscript.

## Competing interests

The authors declare no competing interests.

## Additional information

**Supplementary information** is available for this paper at https://doi.org/10.1038/s41556-019-0291-8.

**Reprints and permissions information** is available at www.nature.com/reprints.

**Correspondence and requests for materials** should be addressed to J.Y.

**Publisher's note:** Springer Nature remains neutral with regard to jurisdictional claims in published maps and institutional affiliations.

## Methods

**Reagents, antibodies and DNA constructs.** The primary antibodies used include: anti-SNAI1 (CST, 3879; 1:200 for immunostaining, 1:1,000 for immunoblotting), mouse anti-SNAI1 EC3 monoclonal antibody (a gift from A. G. de Herreros, Institut Hospital del Mar d'Investigacions Mèdiques; 1:25 for immunostaining), anti-Twist1 (Santa Cruz, sc-81417; 1:50 for immunostaining, 1:1,000 for immunoblotting), anti-E-cadherin (BD, 610182; 1:200 for immunostaining); anti-fibronectin (Sigma, F3648; 1:200 for immunostaining), anti-integrin α5 (Millipore, AB1928; 1:100 for immunostaining), anti-laminin V (a gift from M. Aumailley, University of Cologne; 1:1,000 for immunostaining), anti-PAR3 (Millipore, 07-330; 1:100 for immunostaining, 1:4,000 for immunoblotting), anti-phospho-PKCζ (T560; Abcam, ab62372; 1:100 for immunostaining, 1:2,000 for immunoblotting), anti-vimentin (V9; Santa Cruz, sc-6260, 1:50 for immunostaining), anti-β-TrCP (Santa Cruz, sc-390629, sc-166492; 1:500 for immunoblotting), anti-PKCι (Genetex, GTX102900; 1:1,000 for immunoblotting), anti-cytokeratin 8 (TROMA-I; DSHB; 1:10 for immunostaining), anti-cytokeratin (Covance, PRB-160P; 1:200 for immunostaining), anti-aPKC (Santa Cruz, sc-216; 1:100 for immunostaining, 1:5,000 for immunoblotting), anti-CD45 (BD, 550539; 1:100 for immunostaining), anti-pan-cytokeratin (Abcam, ab9377; 1:200 for immunostaining), anti-phospho-SNAI1(S249) (rabbit polyclonal antibody generated by Abgent; 1:500 for immunoblotting) and anti-GAPDH (Genetex, GTX100118; 1:20,000 for immunoblotting). The secondary fluorescent antibodies used include anti-mouse, -rabbit and -rat conjugated to Alexa Fluor 488, 546 and 647 (Life Technologies). The secondary horseradish peroxidase-conjugated antibodies used include anti-mouse and anti-rabbit (Jackson Immunoresearch). Doxycycline and ML7 were purchased from Sigma. PZ09 was synthesized by Reagency. All Plasmids such as pWZL-Blast-*SNAI1*, pFASTBac-*SNAI1* and pLKO-Tet-*On-SNAI1* were generated from complementary DNA by PCR. Mutants were constructed using a site-directed mutagenesis kit (Agilent Technologies). All shRNA constructs were purchased from Sigma and their sequences are listed in Supplementary Table 1.

**Cell culture.** MCF10DCIS cells were grown in DMEM/F12 media supplemented with 5% horse serum, 20 ng ml$^{-1}$ human epidermal growth factor (EGF), 10 μg ml$^{-1}$ insulin, 0.5 μg ml$^{-1}$ hydrocortisone, 1% penicillin and streptomycin, and 100 ng ml$^{-1}$ cholera toxin (Sigma Aldrich). Caco2 cells were cultured in MEM media supplemented with 20% fetal bovine serum, penicillin and streptomycin. Sf9 cells were grown in Sf-900 II SFM media (Gibco) in shaking cultures at 27 °C. To generate stable gene-knockdown cells, shRNA lentiviruses (human PAR3, mouse Par3 and human SNAI1 MISSION shRNA; Sigma) were transduced into target cells with 6 μg ml$^{-1}$ protamine sulphate. To generate stable gene-overexpressing cells, retroviruses (pWZL-Blast-SNAI1, SNAI1 S249A and SNAI1 S249E mutant) were infected into target cells with 6 μg ml$^{-1}$ protamine sulphate. The infected cells were then selected for with 2 μg ml$^{-1}$ puromycin or blasticidin.

**3D cell culture.** Caco2 cells were grown in 3D cell culture as previously described[51]. Briefly, Caco2 cells were seeded on Matrigel (Growth Factor Reduced Matrigel, BD Biosciences) in 2% Matrigel MEM media supplemented with 20% fetal bovine serum, penicillin and streptomycin.

**Inducible *SNAI1* and *TWIST1* transgenic mice.** All animal care and experiments were performed in accordance with the animal protocol approved by the Institutional Animal Care and Use Committee of the University of California, San Diego. This study is compliant with all relevant ethical regulations regarding animal research. TetON-Snai1 and -Twist1 mice were generated using a site-specific single copy integration strategy to insert a single copy of the transgene in the *Col1A* locus[52]. Inducible SNAI1 and TWIST1 mice were generated by crossing TetON-Snai1 and TetON-Twist1 mice with ROSA-rtTA mice. The expression of SNAI1 and TWIST1 was induced by doxycycline (1 μg ml$^{-1}$) treatment.

**Isolation and 3D cultures of primary MEOs.** Three-dimensional MEO cultures were prepared as previously described[53]. Briefly, all mammary glands were harvested from ROSA-rtTA/TetON-Snai1 or ROSA/rtTA/TetON-Twist1 transgenic mice, minced and digested with 25 ml collagenase solution in DMEM/F12 media with 2% BSA, 25 μg ml$^{-1}$ gentamicin, 5 μg ml$^{-1}$ insulin, 0.1 g collagenase A (Roche) and 0.2% trypsin in the flask for 30 min at 37 °C. MEOs were isolated by differential centrifugations (pulse up to 1,500 r.p.m. in 10 ml DMEM/F12 media) and resuspended in DMEM/F12 media. For 3D cultures, MEOs were embedded in 50% Matrigel (BD) and cultured in 3D growth media (DMEM/F12 media supplemented with 1% insulin-transferrin-sodium selenite (ITS, Sigma), 25 ng ml$^{-1}$ EGF, 50 ng ml$^{-1}$ neuregulin (NRG, R&D Systems), 1% penicillin and streptomycin) in an eight-well chamber slide (Nunc Lab-Tek). For 2D cultures, MEOs were seeded in a regular culture plate and cultured in growth media with 2% fetal calf serum.

**Immunostaining of MEOs.** We used a protocol adapted from a previously described method[54]. Briefly, MEOs were fixed in 4% paraformaldehyde for 20 min at room temperature and permeabilized with PBS containing 0.2% Triton X-100 and 0.1% BSA for 10 min at 4 °C, washed three times with PBS containing 100 mM glycine and then incubated in PBS containing 5 mM EDTA, 1 mM NaVO$_4$, 1.5 mM

NaF for 1–2 d at 4 °C to remove the Matrigel. Samples were blocked with 10% goat serum in immunobuffer (PBS containing 0.1% Tween 20 and 1% BSA), incubated overnight with primary antibodies in immunobuffer, washed three times with immunobuffer, incubated with secondary antibodies for 1 h, washed three times with immunobuffer and mounted with 4,6-diamidino-2-phenylindole (DAPI)-containing mounting medium (Vector). Images were acquired using an Olympus FV1000 confocal microscope and analysed using ImageJ software.

**Immunoblotting and immunoprecipitation.** MEOs were isolated in cell recovery solution (Corning) to extract protein from 3D cultures as per the manufacturer's protocol. MEOs were lysed with RIPA buffer (50 mM Tris–HCl, 1% NP-40, 0.2% SDS, 0.5% sodium deoxycholate, 150 mM NaCl and 10 mM NaF). Immunoprecipitations were prepared as previously described[55]. Briefly, MCF10A cells, Caco2 cells and organoids were lysed with IP lysis buffer (20 mM Tris–HCl, 1% Triton X-100, 10 mM MgCl$_2$, 10 mM KCl, 2 mM EDTA, 1 mM NaF, 1 mM sodium orthovanadate, 2.5 mM β-6-glycerophosphate, 10% glycerol, pH 7.5). Antibodies to SNAI1 and PKCζ were conjugated to protein G beads (Invitrogen), crosslinked using disuccinimidyl suberate (Thermo Scientific Pierce) as per the manufacturer's protocol, incubated with lysates overnight at 4 °C, washed five times with IP lysis buffer supplemented with 200 mM NaCl and eluted using 50 mM dithiothreitol LDS sample buffer at 70 °C for 10 min.

**Real-time PCR.** RNA was extracted from cells and MEOs using Trizol reagent (Thermo Fisher Scientific). Random hexamer primers and a cDNA reverse transcription kit (Applied Biosystems) were used to generate cDNA. All of the qPCR primer sequences are listed in Supplementary Table 2. Expression values were generated using $\Delta\Delta C_t$ values normalized to GAPDH and HPRT. The experiments were performed in triplicate, both biological and technical, using the 7500 Fast (Applied Biosystems) and CFX Connect (Bio-Rad) real-time PCR detection systems. For each comparison, unpaired two-tailed Student's *t*-tests with Welch's correction were used to determine statistical significance.

**In vitro kinase assay.** Human Myc-His$_6$-SNAI11 WT and S249A were expressed and pulled down from Sf9 insect cells using Ni-NTA agarose resin. Human PKCζ was expressed and purified from Sf9 insect cells. Phosphorylation reactions were carried out using 1 μg purified SNAI1, 200 ng purified PKCζ in 20 mM HEPES buffer (pH 7.4), 5 mM MgCl$_2$ and 500 μM ATP at 30 °C for 1 h, in the presence of 20 μM PZ09 or the vehicle control (DMSO).

**aPKC kinase activity fluorescence resonance energy transfer imaging.** Caco2 cells co-transfected with the PKC activity reporter CKAR and mCherry-tagged PKCζ or mCherry-Vec control were plated in 3D organoids culture on 35-mm imaging dishes for 2 d and imaged in HanK's balanced salt solutions supplemented with 1 mM CaCl$_2$. To analyse PKCζ kinase activity, cells were treated with 5 μM PZ09 and the change in fluorescence resonance energy transfer resulting from phosphorylation of the reporter was measured using previously described methods[38].

**Caco2 xenograft mouse model.** GFP-labelled Caco2 cells overexpressing shRFP (5.0 × 10$^6$), shPAR3 no. 3 (0.5 × 10$^6$), shPAR3 no. 4 and shSNAI1 (1.0 × 10$^6$) that were suspended in 100 μl Matrigel (BD Biosciences) were injected bilaterally into the flanks of seven-week-old female BALB/c nude mice. Mice were euthanized and tumour burden was analysed at six weeks after tumour cell injection. Mice were dissected and tumour invasion was assessed in situ using a fluorescent dissection scope (Leica Microsystems).

**Isolation and analysis of circulating tumour cells.** Peripheral blood was obtained from tumour-bearing mice via intracardiac puncture at the termination of the experiment. Red blood cells were removed by dextran solution, RBC lysis buffer and CD45 magnetic beads (Invitrogen). The remaining cells were fixed in 2% paraformaldehyde. The cells were then spun onto slides using a cytospin and stained with rat anti-CD45 and rabbit anti-pan-cytokeratin (Abcam) antibodies, followed by DAPI nuclear staining. Images were acquired using an Olympus FV1000 confocal microscope and analysed using ImageJ software.

**Tumour TMAs.** TMAs were purchased from US Biomax Inc (BB08015, BR246a and T087b). A total of 48 duplicate TMA samples were used: 6 normal breast, 21 ductal intraepithelial neoplasia and 21 invasive ductal carcinoma. For the retrospective analysis, 371 Stage 2 TMAs were purchased from the National Cancer Institute Cancer Diagnosis Program. The TMA contains human tissues that were obtained with informed consent according to US federal law and are exempt from Institutional Review Board review by the University of California, San Diego Human Research Protections Program. Immunostaining for SNAI1 and PAR3 was performed as described above. TMAs were concurrently imaged by confocal microscopy. All samples were scored blindly according to the following method. Score = qp + qs, where the proportion of immune-positive cells were assigned a qp of 1 for 0–4%, 2 for 5–19%, 3 for 20–39%, 4 for 40–59%, 5 for 60–79% and 6 for 80–100%, and strength of staining (qs) was scored as: 0 for negative, 1 for weak expression, 2 for intermediate expression and 3 for strong expression[55,56]. Immunohistochemistry for SNAI1 and PAR3 were performed.

**Statistics and reproducibility.** Statistical analysis was performed using GraphPad Prism Software. All *P* values were derived from Student's *t*-tests comparing two groups using unpaired two-tailed analysis with Welch's correction or paired two-tailed *t*-tests, unless otherwise noted. Error bars denote the s.d. unless otherwise noted. Statistical significance was defined as $P < 0.05$ with regard to the null hypothesis. All qualitative data shown using representative data were repeated in at least three independent biological replicates. The correlation of the SNAI1 and PAR3 levels in human breast-cancer patients was analysed using a $\chi^2$ test.

**Reporting Summary.** Further information on research design is available in the Nature Research Reporting Summary linked to this article.

## Data availability

The source data for Figs. 1–8 and Supplementary Figs. 1–6 are provided in Supplementary Table 3. All other data are available from the authors on reasonable request.

## References

51. Debnath, J., Muthuswamy, S. K. & Brugge, J. S. Morphogenesis and oncogenesis of MCF-10A mammary epithelial acini grown in three-dimensional basement membrane cultures. *Methods* **30**, 256–268 (2003).
52. Beard, C., Hochedlinger, K., Plath, K., Wutz, A. & Jaenisch, R. Efficient method to generate single-copy transgenic mice by site-specific integration in embryonic stem cells. *Genesis* **44**, 23–28 (2006).
53. Fata, J. E. et al. The MAPK(ERK-1,2) pathway integrates distinct and antagonistic signals from TGFα and FGF7 in morphogenesis of mouse mammary epithelium. *Dev. Biol.* **306**, 193–207 (2007).
54. Lee, G. Y., Kenny, P. A., Lee, E. H. & Bissell, M. J. Three-dimensional culture models of normal and malignant breast epithelial cells. *Nat. Methods* **4**, 359–365 (2007).
55. Yin, J. et al. Association of PKCζ expression with clinicopathological characteristics of breast cancer. *PLoS ONE* **9**, e90811 (2014).
56. Amaral, T., McKenna, S. J., Robertson, K. & Thompson, A. Classification and immunohistochemical scoring of breast tissue microarray spots. *IEEE Trans. Biomed. Eng.* **60**, 2806–2814 (2013).

# nature research

| | |
|---|---|
| Corresponding author(s): | Jing Yang |
| Last updated by author(s): | Dec 21, 2018 |

# Reporting Summary

Nature Research wishes to improve the reproducibility of the work that we publish. This form provides structure for consistency and transparency in reporting. For further information on Nature Research policies, see Authors & Referees and the Editorial Policy Checklist.

## Statistics

For all statistical analyses, confirm that the following items are present in the figure legend, table legend, main text, or Methods section.

| n/a | Confirmed | |
|---|---|---|
| ☐ | ☒ | The exact sample size ($n$) for each experimental group/condition, given as a discrete number and unit of measurement |
| ☐ | ☒ | A statement on whether measurements were taken from distinct samples or whether the same sample was measured repeatedly |
| ☐ | ☒ | The statistical test(s) used AND whether they are one- or two-sided<br>*Only common tests should be described solely by name; describe more complex techniques in the Methods section.* |
| ☐ | ☒ | A description of all covariates tested |
| ☐ | ☒ | A description of any assumptions or corrections, such as tests of normality and adjustment for multiple comparisons |
| ☐ | ☒ | A full description of the statistical parameters including central tendency (e.g. means) or other basic estimates (e.g. regression coefficient) AND variation (e.g. standard deviation) or associated estimates of uncertainty (e.g. confidence intervals) |
| ☒ | ☐ | For null hypothesis testing, the test statistic (e.g. $F$, $t$, $r$) with confidence intervals, effect sizes, degrees of freedom and $P$ value noted<br>*Give P values as exact values whenever suitable.* |
| ☒ | ☐ | For Bayesian analysis, information on the choice of priors and Markov chain Monte Carlo settings |
| ☒ | ☐ | For hierarchical and complex designs, identification of the appropriate level for tests and full reporting of outcomes |
| ☒ | ☐ | Estimates of effect sizes (e.g. Cohen's $d$, Pearson's $r$), indicating how they were calculated |

*Our web collection on statistics for biologists contains articles on many of the points above.*

## Software and code

Policy information about availability of computer code

| Data collection | No commercial, open source or custom code were used to collect the data. |
|---|---|
| Data analysis | GraphPad Prism (version 7.0)<br>ImageJ (version 1.43u) |

For manuscripts utilizing custom algorithms or software that are central to the research but not yet described in published literature, software must be made available to editors/reviewers. We strongly encourage code deposition in a community repository (e.g. GitHub). See the Nature Research guidelines for submitting code & software for further information.

## Data

Policy information about availability of data

All manuscripts must include a data availability statement. This statement should provide the following information, where applicable:
- Accession codes, unique identifiers, or web links for publicly available datasets
- A list of figures that have associated raw data
- A description of any restrictions on data availability

Source data for figures 1-8 and supplementary figures 1-6 are provided with the paper.

# Field-specific reporting

Please select the one below that is the best fit for your research. If you are not sure, read the appropriate sections before making your selection.

☒ Life sciences ☐ Behavioural & social sciences ☐ Ecological, evolutionary & environmental sciences

# Life sciences study design

All studies must disclose on these points even when the disclosure is negative.

| | |
|---|---|
| Sample size | Appropriate retrospective analyses were carried out to determine at minimum a 95% confidence interval with at least 3 independent experiments.<br>For TMA analysis, sample size was predicted on sample availability and tumor stages. Tissue microarrays (TMAs) were purchased from US Biomax Inc (BB08015, BR246a, T087b). A total of 48 duplicates TMA samples included 6 normal breast, 21 ductal intraepithelial neoplasia and 21 invasive ductal carcinoma. For retrospective analysis, 371 Stage-2 TMA were also purchased from National Cancer Institute Cancer Diagnosis Program. The TMA contained human tissues obtained with informed consent according to US federal law and are exempt from Institutional Review Board review by the University of California, San Diego Human Research Protections Program.<br>For mouse experiment, sample size was calculated by power analysis including effect size, type 1 error (p=0.05), Power (80%), two-tailed analysis, and standard deviation.<br>Statistical analysis was performed using GraphPad Prism Software. All P values were derived from Student's test comparing two groups using unpaired two-tailed analysis with Welch's correction, unless otherwise noted. Error bars denote standard deviation unless otherwise noted. Statistical significance was defined as P < 0.05, with regard to the null hypothesis. All qualitative data shown using representative data were repeated in at least 3 independent biological replicates. Correlation of SNAI1 and PAR3 levels in human breast cancer patients was analysed using a $\chi 2$ test. |
| Data exclusions | No data exclusions were applied. |
| Replication | Each experiment performed at minimum in biologic triplicates to unsure the reproducibility of the results. Per experiment, these approaches are described in the figure legends. All attempts at replication were successful. |
| Randomization | In all cell culture experiments, the same starting cell lines or primary cells harvested from mice were seeded in a number of plates and each plate is randomly assigned as control v.s. treatment groups.<br>For mouse experiments, all littermate mice were randomly divided into groups for implantation of different tumor cell lines . |
| Blinding | TMA samples were scored blindly prior to analysis.<br>Mouse tumor size, weight and lung metastasis lesions were quantified blindly. |

# Reporting for specific materials, systems and methods

We require information from authors about some types of materials, experimental systems and methods used in many studies. Here, indicate whether each material, system or method listed is relevant to your study. If you are not sure if a list item applies to your research, read the appropriate section before selecting a response.

## Materials & experimental systems

| n/a | Involved in the study |
|---|---|
| ☐ | ☒ Antibodies |
| ☐ | ☒ Eukaryotic cell lines |
| ☒ | ☐ Palaeontology |
| ☐ | ☒ Animals and other organisms |
| ☒ | ☐ Human research participants |
| ☒ | ☐ Clinical data |

## Methods

| n/a | Involved in the study |
|---|---|
| ☒ | ☐ ChIP-seq |
| ☒ | ☐ Flow cytometry |
| ☒ | ☐ MRI-based neuroimaging |

## Antibodies

| | |
|---|---|
| Antibodies used | anti-SNAI1 (CST, 3879), anti-SNAI1 EC3 monoclonal antibody (a kind gift from Dr. A. Garcia de Herreros, Institut Hospital del Mar d'Investigacions Mèdiques, Barcelona, Spain,), anti-Twist1 (Santa Cruz, sc-81417), anti-E-cadherin (BD, 610182), anti-Fibronectin (Sigma, F3648), anti-integrin α5 (Millipore, AB1928), anti-laminin V (a kind gift from Dr. M. Aumailley, University of Cologne, Germany,), anti-PAR3 (Millipore, 07-330), anti-phospho-PKCζ (T560) (Abcam, ab62372), anti-Vimentin, V9 (Santa Cruz, sc-6260), anti-β-TrCP (Santa Cruz, sc-390629, sc-166492), anti-PKCι (Genetex, GTX102900), anti-CK8 (cytokeratin-8: TROMA-I, DSHB), anti-CK5 (cytokeratin-5, Covance, PRB-160P), anti-PKCζ (Santa Cruz, sc-216), anti-CD45 (BD, 550539), anti-pan-cytokeratin (Abcam, ab9377), anti-phospho-SNAI1(S249) (rabbit polyclonal antibody generated by our lab), and anti-GAPDH (Genetex, GTX100118). |
| Validation | Rabbit anti-SNAI1 (CST, 3879, 1:200 for immunostaining, 1:1000 for immunoblotting), mouse anti-SNAI1 EC3 monoclonal antibody (a kind gift from Dr. A. Garcia de Herreros, Institut Hospital del Mar d'Investigacions Mèdiques, Barcelona, Spain, 1:25 for immunostaining), mouse anti-Twist1 (Santa Cruz, sc-81417, 1:50 for immunostaining, 1:1000 for immunoblotting), mouse anti-E-cadherin (BD, 610182, 1:200 for immunostaining), rabbit anti-Fibronectin (Sigma, F3648, 1:200 for immunostaining), rabbit anti-integrin α5 (Millipore, AB1928, 1:100 for immunostaining), rabbit anti-laminin V (a kind gift from Dr. M. Aumailley, University of Cologne, Germany, 1:1000 for immunostaining), rabbit anti-PAR3 (Millipore, 07-330, 1:100 for immunostaining, 1:4000 for immunoblotting), rabbit anti-phospho-PKCζ (T560) (Abcam, ab62372, 1:100 for immunostaining, 1:2000 for immunoblotting), mouse anti-Vimentin, V9 (Santa Cruz, sc-6260, 1:50 for immunostaining), mouse anti-β-TrCP (Santa Cruz, sc-390629, sc-166492, 1:500 for immunoblotting), rabbit anti-PKCι (Genetex, GTX102900, 1:1000 for immunoblotting), rat anti- |

CK8 (cytokeratin-8: TROMA-I, DSHB, 1:10 for immunostaining), rabbit anti-CK5 (cytokeratin-5, Covance, PRB-160P, 1:200 for immunostaining), goat anti-PKCζ (Santa Cruz, sc-216, 1:100 for immunostaining, 1:5000 for immunoblotting), rat anti-CD45 (BD, 550539, 1:100 for immunostaining), rabbit anti-pan-cytokeratin (Abcam, ab9377, 1:200 for immunostaining), anti-phospho-SNAI1(S249) (rabbit polyclonal antibody generated by our lab, 1:500 for immunoblotting), and rabbit anti-GAPDH (Genetex, GTX100118, 1:20000 for immunoblotting).

# Eukaryotic cell lines

Policy information about [cell lines](cell lines)

| | |
|---|---|
| Cell line source(s) | MCF10A, 293T and Caco2 cells were directly obtained from ATCC. MCF10DCIS was obtained directly from Dr. Fred Miller, who derived this cell line. |
| Authentication | All cell lines were authenticated by STR profiling. |
| Mycoplasma contamination | We routinely test all cell lines used using Lonza MycoAlert Mycoplasma detection kit and found them to be negative for mycoplasma consistently. |
| Commonly misidentified lines (See [ICLAC](ICLAC) register) | No commonly misidentified cell lines were used. |

# Animals and other organisms

Policy information about [studies involving animals](studies involving animals); [ARRIVE guidelines](ARRIVE guidelines) recommended for reporting animal research

| | |
|---|---|
| Laboratory animals | MEOs were collected from 2-month old inducible SNAI1 and Twist1 mice, generated by crossing TetON-SNAI1 and TetON-Twist1 mice with ROSA-rtTA mice.<br>For xenograft experiments, 7-week-old female BALB/c nude mice were used. |
| Wild animals | The study did not involve wild animals. |
| Field-collected samples | The study did not involve samples collected from the field. |
| Ethics oversight | All animal care and experiments were performed in accordance with the animal protocol approved by the Institutional Animal Care and Use Committee of the University of California, San Diego. |

Note that full information on the approval of the study protocol must also be provided in the manuscript.